ACADEMIC PRESS

Available online at www.sciencedirect.com

SCIENCE DIRECT®

Journal of Computational Physics 186 (2003) 136–177

JOURNAL OF COMPUTATIONAL PHYSICS

www.elsevier.com/locate/jcp

An Eulerian method for computation of multimaterial impact with ENO shock-capturing and sharp interfaces

H.S. Udaykumar [a,*], L. Tran [a], D.M. Belk [b], K.J. Vanden [b]

[a] *Department of Mechanical and Industrial Engineering, University of Iowa, Iowa City, IA 52242-1527, USA*
[b] *USAF Research Laboratory (AFRL/MNAC), Eglin AFB, Eglin, FL 32542, USA*

Received 18 July 2002; received in revised form 25 November 2002; accepted 16 January 2003

Abstract

A technique is presented for the numerical simulation of high-speed multimaterial impact. Of particular interest is the interaction of solid impactors with targets. The computations are performed on a fixed Cartesian mesh by casting the equations governing material deformation in Eulerian conservation law form. The advantage of the Eulerian setting is the disconnection of the mesh from the boundary deformation allowing for large distortions of the interfaces. Eigenvalue analysis reveals that the system of equations is hyperbolic for the range of materials and impact velocities of interest. High-order accurate ENO shock-capturing schemes are used along with interface tracking techniques to evolve sharp immersed boundaries. The numerical technique is designed to tackle the following physical phenomena encountered during impact: (1) high velocities of impact leading to large deformations of the impactor as well as targets; (2) nonlinear wave-propagation and the development of shocks in the materials; (3) modeling of the constitutive properties of materials under intense impact conditions and accurate numerical calculation of the elasto-plastic behavior described by the models; (4) phenomena at multiple interfaces (such as impactor–target, target–ambient and impactor–ambient), i.e. both free surface and surface–surface dynamics. Comparison with Lagrangian calculations is made for the elasto-plastic deformation of solid material. The accuracy of convex ENO scheme for shock capturing, with the Mie–Gruneisen equation of state for pressure, is closely examined. Good agreement of the present finite difference fixed grid results is obtained with exact solutions in 1D and benchmarked moving finite element solutions for axisymmetric Taylor impact.

Keywords: Moving boundaries; Impact; Multimaterial flows; High-strain rate

1. Introduction

This paper describes a method for the simulation of high-strain rate, large deformation problems resulting from high-velocity impact of solids [1,2]. The deformation of the media is accompanied by prop-

* Corresponding author. Tel.: 1-319-384-0832; fax: 1-319-335-6086.
E-mail address: ush@engineering.uiowa.edu (H.S. Udaykumar).

0021-9991/03/$ - see front matter
doi:10.1016/S0021-9991(03)00027-5

agation of elasto-plastic waves in the material. Wave-propagation in the impacting media is highly nonlinear and involves localized phenomena such as shear bands, crack propagation, and wave refraction. In addition, the stress and strain fields are related through nonlinear elasto-plastic yield surfaces, the models for which must be included in the governing equations. The two key challenges to the numerical analysis of physical problems of this type are the presence of large gradients in the flow of the material and the large deformations of the material boundaries. These two aspects are dealt with in this work using methods that are adapted from computational fluid dynamics, viz.:

1. Modern hydrodynamic shock-capturing Essentially Non-Oscillatory (ENO) schemes [3–6] are applied to compute the wave-propagation phenomena in the material. The discretization is performed on a fixed Cartesian mesh, where implementation of high-order ENO schemes is straightforward.
2. A Sharp Interface Approach [7,8] is applied to propagate the arbitrarily deforming material boundaries through the fixed mesh without smearing of the material boundary, a problem that is inherent in purely Eulerian fixed grid methods. The present method, therefore, treats the moving material boundary as a sharp entity. Since the grid remains unchanged as the boundary evolves, large deformations of the boundary can be handled.

Typically, high-velocity impact calculations have been performed by "hydrocodes". Such codes may be based on a Lagrangian formulation, such as in EPIC and DYNA, where a moving unstructured mesh is used to follow the deformation, or an Eulerian formulation, such as in CTH, where a fixed mesh is used and the boundaries are tracked through the mesh. Benson [9] provides an extensive review of the formulation, modeling and computational techniques employed by these large-scale computer codes.

Lagrangian and Arbitrary Lagrangian–Eulerian (ALE) methods [10] for the simulation of problems with severe material deformation have been applied extensively in the solid mechanics community. For example, Camacho and Ortiz [11,12] have developed a Lagrangian finite element impact dynamics model for deformation of brittle materials [11], and ductile penetration [12]. Their approach is based on adaptive meshing, explicit contact/friction algorithm, and rate-dependent plasticity. In moving mesh methods, considerable complexity is enjoined by the need for mesh management, i.e., in maintaining an adequately refined mesh with good mesh quality. For very severe deformations, meshless methods [13–16], or a combination of finite element methods with embedded boundary tracking and local enrichment [17–19] have emerged as attractive alternatives in recent years. In these methods, one either entirely dispenses with a mesh or the mesh does not distort as the embedded boundary (such as a crack) propagates through the mesh. Hence, one is freed from the burden of mesh management due to large boundary deformations. On the other hand, in the fluid mechanics community, moving boundary problems involving large material distortion have been commonly dealt with for decades using methods that rely on advecting boundaries through fixed grids, using an Eulerian (as in the Volume-of-Fluid approach of Hirt and Nichols [20]) or mixed Eulerian–Lagrangian (as in the Immersed Boundary Method of Peskin [21]) formulation. Methods that have relied on moving meshes that conform to boundaries have been useful in problems involving moderate interface deformation [22,23]. Methods that entirely dispense with a mesh, such as the Lagrangian SPH (Smooth Particle Hydrodynamics [24,25]), are yet to develop into strong alternatives to mesh-based methods. Current research issues in such methods include stability [26–29], accurate treatment of boundary conditions [30–32], and the efficient solution of incompressible flows [33]. In many moving boundary problems in fluid dynamics, e.g., the dynamics of droplets, jets or surface waves [34], interaction of flows with complex solid–liquid interfaces [35], etc., grid-based Eulerian methods been have been preferred, due to the ability to disconnect the deforming interface from the computational mesh.

Hitherto, Eulerian methods have been applied to study material deformation by some researchers by adapting techniques in the arsenal of computational fluid dynamics. For example, Trangenstein [36–38], Trangenstein and Pember [39], and Miller and Colella [40] have adopted Godunov's method and ideas developed in modern computational fluid dynamics to handle multimaterial impact as a Riemann type problem with second-order accuracy. Benson and coworkers [41,42] have applied Eulerian methods to

study the collapse of voids in materials under impact loading. The methods presented by Benson and coworkers, although based on an Eulerian fixed mesh setting are of the Lagrangian-plus-remap type. In these methods, the material deformation calculations are split into two steps, first the material is evolved by a Lagrangian step which deforms nodes to new positions and then the field is mapped back to the fixed Eulerian mesh and the new interfaces reconstructed by a Young's reconstruction. Thus, within each cell a fraction can be solid and the rest void. This combination of Lagrangian and Eulerian steps circumvents the smearing of the interfaces inherent in purely Eulerian methods. Purely Eulerian methods, if constructed based on volume fractions, tend to smear interfaces, either due to incidental numerical diffusion accompanying the material advection scheme or by intentionally spreading the interfaces over the mesh in order to mitigate the stiffness of the problem in the presence of large material discontinuities [43]. In the Lagrangian-plus-remap methods, the mixed cells have to be treated using a mixture formalism [44] to redistribute the stresses and strains between the material and void spaces. Proper equilibration of stresses within the cell has to be enforced to prevent the voids from exhibiting spurious strength and to prevent stress boundary layers from building up at free surfaces. Benson [44] addresses the pros and cons of the choices available to treat the subcell stress and strain fields using a mixture theory. This approach has been used to good effect in the solution of mesoscale response of materials in shock compression [45] and void collapse [42]. In particular, Menikoff and coworkers [45,46] have employed such Eulerian methods to study the dynamic response of granular energetic materials (HMX) to impact loading. Detailed modeling of the interaction of the grains and initiation of detonation due to collapse of voids and formation of hot spots in the material has been performed.

In contradistinction to the above Eulerian methods based on treating the material as a fraction of a cell and advecting mixed materials within cells, computational fluid dynamics techniques have recently been developed that solve the governing equations on a fixed mesh, while maintaining a sharp representation of material boundaries. Applications of such sharp interface methods have included calculations of dendritic solidification of materials [47–51], fluid–solid interactions [7,8,52,53], droplet/bubble dynamics [54,55], etc. This class of "sharp interface" methods may be based on a mixed Eulerian–Lagrangian framework [7,8,51] or a purely Eulerian framework [52,48]. In both frameworks, the governing equations are solved in Eulerian form on a fixed mesh. The distinction lies in the treatment of the immersed boundary. In the former, while the interface is tracked as a curve or surface through the mesh, in the latter case, the interface may be advected as a field variable, typically as a level-set function [56].

There have been research efforts that bear direct relevance to the focus of this paper, i.e., the numerical issues related to propagation of shock waves in condensed media and interactions of media during impact. The shock-capturing methods that were developed for gas dynamics have been extended to condensed media for application to high-velocity (in liquids) or high-strain rate (in solids) problems where nonlinear wave-propagation phenomena are important. Application of hydrodynamic shock-capturing techniques to materials with general equation of state has been presented by Arienti et al. [57], Fedkiw et al. [52,58], Glaister [59], and Miller and Puckett [61]. Glaister [59] and Arienti et al. [57] employ the Roe scheme and an approximate Riemann solver to capture shocks. While the former work is restricted to gases and one-dimension with a general convex equation of state, the latter deals with solid materials with the Mie–Gruneisen equation of state for the pressure, but they solve the Euler equations for the flow of the condensed material, i.e. the strength of the solid is not considered. Arienti et al. [57] have also investigated two-dimensional problems in that setting. Following Dukowicz's [60] application of an approximate Riemann solver to capture contact discontinuities, Miller and Puckett [61] also presented an approximate Riemann solver for multimaterials with the general e.o.s. where the material interfaces can lie within cells. They treated the multiple materials as a mixture within each cell (i.e. volume fractions) but did not resort to the Lagrangian-plus-remap approach. Material strength was not considered. The discrete Riemann solver for their formulation was fairly challenging to develop, particularly at the faces of the mixed cells. A simpler approach is the Ghost Fluid Method due to Fedkiw and coworkers [52]. In this method the interface is

treated as a sharp entity that resides on the fixed mesh and appropriate boundary conditions at the interface are applied by extrapolating the field to an extended "ghost" material. This approach leads to a local reduction in order of accuracy at the computational points adjoining the immersed interfaces. However, since such points are few in number, the overall accuracy is still maintained at the high order. The sharp interface method presented by Udaykumar et al. [8,51] does not rely on such an extended field, but is similar in spirit to the Ghost Fluid Method. In the sharp interface method, the boundary conditions are directly applied on the interface and the discretization at the computational nodes near the interface is suitably modified to account for the presence of the interface. Fedkiw et al. [58] have applied the ENO schemes to study the propagation of shocks in media where the pressure is governed by a variety of equations of state (gases and liquids). Their results show that the ENO scheme can accurately handle shock formation in such systems. Furthermore, the known weakness of the ENO scheme in capturing weak discontinuities in pressure, particularly contact discontinuities (zero pressure jump) is addressed. The smearing of the contact discontinuity (interface) is eliminated through the ghost-fluid approach.

Here, we describe the development of a mixed Eulerian–Lagrangian numerical solution technique for the simulation of high-speed multimaterial impact. Of particular interest is the interaction of solid impactors with targets. This problem is important in applications such as munition–target interactions, geological impact dynamics, shock-induced materials processing such as powder compaction, and formation of shaped charges upon detonation and their subsequent interaction with targets [1,2]. We present a numerical technique that can handle the following physical phenomena typical of impact problems:

(1) High particle velocities leading to large deformations of the impactor as well as targets.
(2) Nonlinear wave-propagation leading to development of shocks in the systems. It is necessary to solve the system of hyperbolic equations by including the material strength and an appropriate e.o.s. for pressure.
(3) High sound speeds relative to the particle speed in the condensed media, contributing to numerical stiffness. In other words, materials that are "nearly incompressible".
(4) Modeling of the constitutive properties of materials under intense impact conditions and accurate numerical calculation of the elasto-plastic behavior of the stressed materials.
(5) Phenomena at multiple interfaces (such as impactor–target, target–ambient, and impactor–ambient), i.e., both free surface and surface–surface dynamics.

The equations governing the material deformation are solved in an Eulerian setting on a fixed Cartesian mesh. The interfaces are tracked as curves on the fixed mesh. Eigenvalue analysis of the governing equations is performed to ensure hyperbolicity in the materials considered and for the impact velocity regime of interest. Modern shock capturing schemes are adapted to the solution of the hyperbolic system of governing equations. The interaction of the embedded boundaries with each other and the evolution of free boundaries is treated by application of appropriate boundary conditions at the resulting material–material and material–void boundaries. The interaction of the interfaces with the computational mesh and the ENO discretization of the equations of flow in the presence of the moving boundaries is described. A detailed study of the performance of Local Lax–Friedrichs ENO schemes [6] is presented for the class of problems of interest in multimaterial impact. Benchmark results are presented for one-dimensional as well as two-dimensional (axisymmetric) problems.

The method presented here is based on a sharp-interface treatment of the moving boundaries. Extension of the method to three-dimensions is straightforward, given the manner in which the governing equations are solved. The finite-difference technique using the ENO scheme assembles fluxes in each direction separately, thereby facilitating extension to 3D. Explicit front tracking of arbitrarily deforming interfaces in 3D is admittedly somewhat challenging. However, while the present method falls in the class of sharp-interface methods, the moving boundaries need not be tracked explicitly as in the present work. Any method that provides sharp tracking of interfaces, such as the level-set method, can be combined with the ENO-based formulation. In ongoing work, we have employed level-set methods to track the sharp moving

interfaces and we will report on this effort in the near future. With level-set tracking and the field-by-field decomposition of ENO, extension of the present approach to 3D is expected to be fairly straightforward.

2. Governing equations

The governing equations are written so that axisymmetric impact of moving boundaries can be considered in the plane, as illustrated in Fig. 1, which shows a Taylor impact model.

The one-dimensional solutions presented later are obtained by reducing the following equations to a system corresponding to uniaxial strain.

The transport equation in vector form is

$$\frac{\partial \vec{Q}}{\partial t} + \frac{\partial F(\vec{Q})}{\partial x} + \frac{\partial G(\vec{Q})}{\partial y} = S(\vec{Q}). \tag{1}$$

The y-axis is the axis of symmetry. For the material deformation problem the vector of independent variables, and the x- (radial) and y-direction (axial) convective flux vectors are given by

$$\vec{Q} = \begin{Bmatrix} \rho \\ \rho u \\ \rho v \\ E \\ \bar{\varepsilon} \\ \tau_{xx} \\ \tau_{yy} \\ \tau_{xy} \end{Bmatrix} \quad F(\vec{Q}) = \begin{Bmatrix} \rho u \\ \rho u^2 + p \\ \rho uv \\ u[E+p] \\ \rho u\bar{\varepsilon} \\ \rho u\tau_{xx} \\ \rho u\tau_{yy} \\ \rho u\tau_{xy} \end{Bmatrix} \quad G(\vec{Q}) = \begin{Bmatrix} \rho v \\ \rho uv \\ \rho v^2 + p \\ v[E+p] \\ \rho v\bar{\varepsilon} \\ \rho v\tau_{xx} \\ \rho v\tau_{yy} \\ \rho v\tau_{xy} \end{Bmatrix}. \tag{2}$$

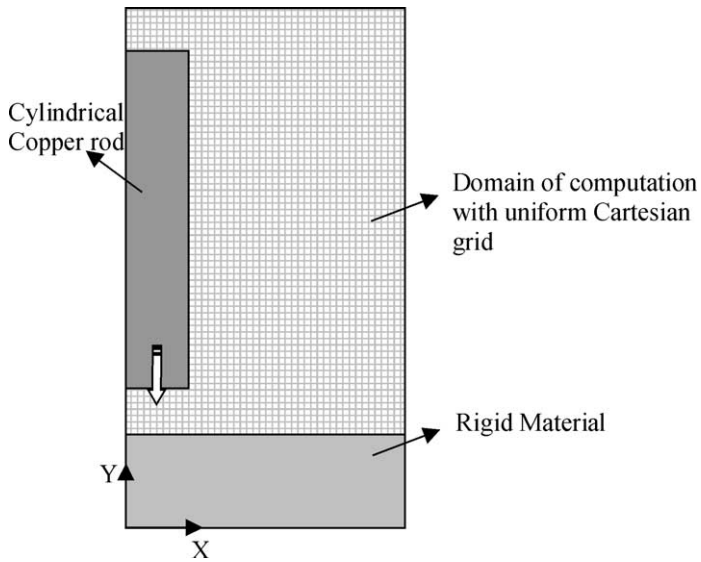

Fig. 1. Computational setup for the study of axisymmetric impact of a copper rod with a rigid surface. This is the standard Taylor impact problem.

In the above equations, ρ is the density, u and v are the x- (radial) and y- (axial) components of the velocity, E is the total energy, p is the pressure, $\bar{\varepsilon}$ is the equivalent plastic strain, and τ_{xx}, τ_{xy}, and τ_{yy} are the components of the deviatoric stresses. In the equation set above the three components of deviatoric stress are chosen as the dependent variables. The equations for the deviatoric stresses have been written by using the Jaumann time derivative in order to maintain frame indifference to rotation. The total stress components are related to the deviatoric stresses through

$$\sigma_{ij} = \tau_{ij} - p\delta_{ij}. \tag{3}$$

The pressure is determined by an equation of state (henceforth e.o.s.) of the form

$$p = \mathrm{eos}(\rho, e). \tag{4}$$

The specific e.o.s. in use here is the Mie–Gruneison e.o.s. [2], appropriate for high-strain rate applications

$$p(e,V) = \frac{c_0^2(V_0 - V)}{[V_0 - s(V_0 - V)]^2} + \frac{\Gamma(V)}{V}\left[e - \frac{1}{2}\left(\frac{c_0(V_0 - V)}{V_0 - s(V_0 - V)}\right)^2\right], \tag{5}$$

where, by definition,

$$e = \frac{E}{\rho} - \frac{u^2 + v^2}{2}, \tag{6}$$

$$V = \frac{1}{\rho}, \tag{7}$$

and the Gruneisen parameter is defined as

$$\Gamma = V\left(\frac{\partial p}{\partial e}\right)_V = \frac{\Gamma_0 \rho_0}{\rho}, \tag{8}$$

where ρ_0 is the density of the unstressed material, c_0 and s are coefficients that relate the shock speed U_s and the particle velocity u_p. The latter is related to the shock velocity by the empirically obtained linear relationship

$$U_\mathrm{s} = c_0 + s u_\mathrm{p}. \tag{9}$$

The source vector is

$$S(\vec{Q}) = \begin{Bmatrix} -\frac{\rho u}{x} \\ \frac{\partial \tau_{xx}}{\partial x} + \frac{\partial \tau_{xy}}{\partial y} + \frac{\tau_{xx} + \tau_{yy} + \tau_{xy}}{x} - \frac{\rho u^2}{x} \\ \frac{\partial \tau_{xy}}{\partial x} + \frac{\partial \tau_{yy}}{\partial y} + \frac{\tau_{xy}}{x} - \frac{\rho u v}{x} \\ S_\mathrm{E} \\ S_{\bar{\varepsilon}} \\ S_{\tau_{xx}} \\ S_{\tau_{yy}} \\ S_{\tau_{xy}} \end{Bmatrix}, \tag{10}$$

where the source term in the equation for energy is

$$S_\mathrm{E} = -\frac{u(E+p)}{x} + \frac{1}{x}\frac{\partial}{\partial x}\left[x(u\tau_{xx} + v\tau_{yy})\right] + \frac{\partial}{\partial y}(u\tau_{xy} + v\tau_{yy}). \tag{11}$$

The source term for equivalent plastic strain depends upon the instantaneous loading condition of the material. For a general elasto-plastic deformation case, it is

$$S_{\bar{\varepsilon}} = \left(\frac{\chi}{1+\Sigma'/3G}\right)\frac{1}{\bar{\sigma}}\left[\tau_{xx}\left(\frac{\partial u}{\partial x}-\frac{u}{x}\right)+\tau_{yy}\left(\frac{\partial v}{\partial y}-\frac{u}{x}\right)+\tau_{xy}\left(\frac{\partial u}{\partial y}+\frac{\partial v}{\partial x}\right)\right], \tag{12}$$

where $\bar{\sigma}=\sqrt{\frac{3}{2}\tau_{ij}\tau_{ij}}$. For plastic loading the switch χ is set to 1, while for elastic loading or unloading from the plastic state it is set to 0. The loading/unloading situation is determined during the computations by the criterion

$$\chi = 0 \quad \text{if } \bar{\sigma} < \Sigma(\varepsilon) \text{ or } \left[\tau_{xx}\left(\frac{\partial u}{\partial x}-\frac{u}{x}\right)+\tau_{yy}\left(\frac{\partial v}{\partial y}-\frac{u}{x}\right)+\tau_{xy}\left(\frac{\partial u}{\partial y}+\frac{\partial v}{\partial x}\right)\right] < 0.$$

$$\chi = 1 \quad \text{otherwise.}$$

The materials investigated in this work include gases (for which the Euler equations apply and all the deviatoric stresses are identically zero) and solids that deform elasto-plastically with a constant hardening rate Σ' in the plastic regime. This latter type of material is of primary interest in the context of impact. However, gamma-law gases are studied to verify and contrast the performance of the numerical method for the different material types. These distinctions are amplified in the section on results.

The source terms in the equations for deviatoric stress components also depend upon the loading condition of the material. For elasto-plastic deformation they are:

$$S_{\tau_{xx}} = \tau_{xx}\left(\frac{\partial u}{\partial x}+\frac{\partial v}{\partial y}\right)+2\Omega_{xy}\tau_{xy}+2G\left[\frac{\partial u}{\partial x}-A-\frac{3}{2}\frac{\chi\tau_{xx}}{\bar{\sigma}^2}\frac{B}{1+\frac{\Sigma'}{3G}}\right], \tag{13}$$

$$S_{\tau_{yy}} = \tau_{yy}\left(\frac{\partial u}{\partial x}+\frac{\partial v}{\partial y}\right)+2\Omega_{yx}\tau_{xy}+2G\left[\frac{\partial v}{\partial y}-A-\frac{3}{2}\frac{\chi\tau_{yy}}{\bar{\sigma}^2}\frac{B}{1+\frac{\Sigma'}{3G}}\right], \tag{14}$$

$$S_{\tau_{xy}} = \tau_{xy}\left(\frac{\partial u}{\partial x}+\frac{\partial v}{\partial y}\right)+\Omega_{xx}\tau_{xy}+\Omega_{xy}\tau_{yy}-\Omega_{xy}\tau_{xx}-\Omega_{yy}\tau_{xy}+2G\left[\frac{1}{2}\left(\frac{\partial u}{\partial y}+\frac{\partial v}{\partial x}\right)-\frac{3}{2}\frac{\chi\tau_{xy}}{\bar{\sigma}^2}\frac{B}{1+\frac{\Sigma'}{3G}}\right]. \tag{15}$$

Again, the switch χ is set to 1 or 0 depending on the type of loading experienced at a given mesh point. Terms containing the rotation components Ω_{ij} appear in the above equations due to the use of the Jaumann rate for the evolution of the stress. In the above

$$A=\frac{1}{3}\left(\frac{\partial u}{\partial x}+\frac{u}{x}+\frac{\partial v}{\partial y}\right), \quad B=\tau_{xx}D'_{xx}+\tau_{zz}D'_{zz}+\tau_{yy}D'_{yy}+2\tau_{xy}D'_{xy} \tag{16}$$

and the components of the rotation tensor are

$$\Omega_{xx}=0, \quad \Omega_{yy}=0, \quad \Omega_{xy}=\frac{1}{2}\left(\frac{\partial u}{\partial y}-\frac{\partial v}{\partial x}\right), \quad \Omega_{yx}=\frac{1}{2}\left(\frac{\partial v}{\partial x}-\frac{\partial u}{\partial y}\right), \tag{17}$$

where D'_{ij} are components of the deviatoric rate of deformation tensor and G is the shear modulus of the material. The elasto-plastic material deformation model is specified through the equivalent stress–strain curve $\bar{\sigma}=\Sigma(\bar{\varepsilon})$ as determined by uniaxial stress experiments. Σ' is the slope of the stress–strain curve. Therefore, we consider the standard Prandtl–Reuss material model and the material properties corresponding to copper are chosen in order to compare our results with benchmarks [12].

In the above, the rate of deformation tensor components D_{ij} and its deviator D'_{ij} are defined as

$$D_{ij} = \frac{1}{2}\left[\frac{\partial u_i}{\partial x_j} + \frac{\partial u_j}{\partial x_i}\right], \tag{18}$$

$$D'_{ij} = D_{ij} - \frac{1}{3}D_{kk}\delta_{ij}, \tag{19}$$

where δ_{ij} is the Kronecker delta.

The governing equations presented above need to be solved subject to appropriate boundary conditions applied at the embedded moving boundaries. The manner in which this interaction between the interfaces and the flow solver is effected is described next.

3. Interface tracking algorithm

The moving boundaries in this work are tracked by advecting markers connected by piecewise polynomial curves. While such explicit tracking allows for a sharp representation of the various boundaries, it does place some limitations on the complexity of boundary topology. For example, we do not compute interface deformations that result in fragmentation. This limitation can be removed by tracking the interfaces using methods such as level-set tracking [56]. Such tracking procedures have been implemented within the present methodology and results on multimaterial interactions using level-set representation and sharp interface physics will be presented in the future. In any event, the precise methodology for tracking boundaries is of secondary importance in this paper, which deals with the simulation of multimaterial interactions and wave-propagation during impact.

Detailed information on interface tracking has been presented in previous papers [8,50,51] and is only briefly described here. The interface is tracked using interfacial markers (or nodes) defined by the coordinates $x(s), y(s)$, where s is the arclength parameter. The spacing between the markers is maintained at some fraction of the grid spacing, $0.5h < ds < 1.5h$. The convention adopted is that as one traverses the interface along the arclength, the material enclosed by the interface lies to the right. This is illustrated in Fig. 2. The functions $x(s) = a_x s^2 + b_x s + c_x$ and $y(s) = a_y s^2 + b_y s + c_y$ are generated. The coefficients $a_{x/y}$, $b_{x/y}$, and $c_{x/y}$ at any interfacial point i are obtained by fitting polynomials through the coordinates $(x_{i-1}, y_{i-1}), (x_i, y_i), (x_{i+1}, y_{i+1})$.

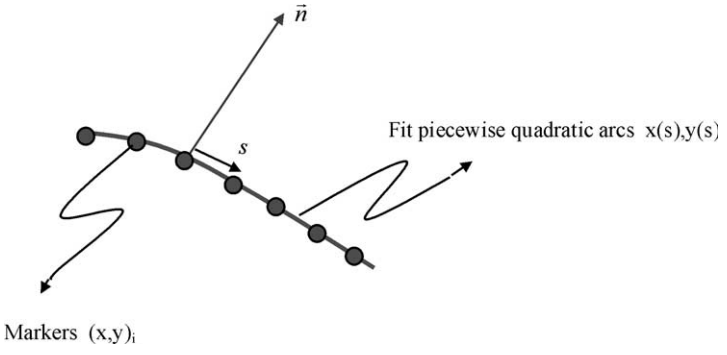

Fig. 2. Illustration of interface properties. The normal to the interface and arclength coordinate are shown.

The coefficients $a_{x/y}$, $b_{x/y}$, and $c_{x/y}$ are stored for each marker point. The normal to the interface then points from the interior to the exterior of the object and is given by the equation

$$\vec{n} = \left(\frac{-y_s}{\sqrt{x_s^2 + y_s^2}}, \frac{x_s}{\sqrt{x_s^2 + y_s^2}} \right). \tag{20}$$

The derivatives x_s, y_s are evaluated using central differencing along the arc length coordinate s.

There are two features that have been included in the tracking procedure for the particular problems solved in this paper:

1. For the Taylor bar problem, there are corners in the bar that need to be advected as kinks in the interface curve without being smoothed.
2. Due to impact, contiguous interfaces are created between impacting surfaces, whose interpenetration needs to be prevented.

The first aspect is dealt with by initially flagging points on the bar (in the axisymmtric case shown in Fig. 1, there are two such points, one at top right of the bar and one at bottom right) as "kinks" and defining the piecewise polynomial curves on the interface separately on either side of the kink. The second aspect is treated in a manner similar to that described by Camacho and Ortiz [11,12] for their Lagrangian calculation. At the beginning of the calculation the interfaces are labelled as the "master" or "disciple". For example, in Fig. 21, the impacting rod is designated the "disciple" and the rigid surface the "master". Then, as the calculation proceeds we detect the proximity of the "disciple" interface to the "master". This is done by checking for the closest "master" marker to any given "disciple" marker. If this distance is below a preset tolerance (which in our case was 0.1 mesh spacing), we declare impact and thereafter the "disciple" interfaces are given the same normal velocity as the closest "master" curve marker. This maintains contiguity of the impacted surfaces during further calculation.

4. Relationship between the interface and grid

Once the interface has been defined the information on its relationship with the grid has to be established. There may be several interfaces (henceforth called objects) immersed in the domain. Each of the objects may enclose material with different transport properties. Therefore, it is necessary to identify which phase each computational point lies in. The procedure for obtaining this and related information has been discussed in detail in [51]. The end result of the procedures are the following pieces of information which are required to set up the discretization scheme for the present method:

1. A list of interfacial computational nodes, i.e., nodes which adjoin the interface.
2. The interface to which the interfacial node is connected, i.e., the identity of the object that passes through the grid cell whose center is the node in question and from which boundary conditions are to be drawn.
3. The material in which each computational point in the mesh lies. This depends on the object in which the node lies. In the event that it lies outside all the objects, i.e., in the void region, the node is flagged as such and no computations are performed at such nodes.
4. Several geometric details such as the shape of the resulting cut-cell, the locations where the interface cuts the cell faces, and where it intersects the cell center lines (the dotted lines shown in Fig. 3). These details of a cell are used in constructing the discrete equations for each interfacial node.

These pieces of information regarding the interface and its relationship to the underlying grid are computed only in a lower-dimensional set of interfacial nodes. Therefore, using local searches and operations and data storage limited to this set of nodes renders dealing with the interface and mesh relationship economical. In practical runs the operations associated with obtaining the interface and mesh information occupy a small fraction of the computing time associated with the field equation solver.

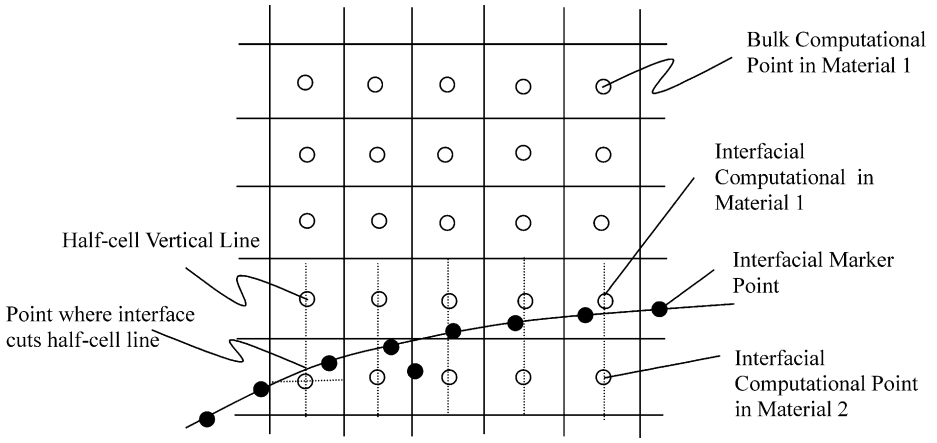

Fig. 3. Information required from the interaction between the interface and the grid to develop the discretization at the interfacial computational points.

5. Numerical method for solving the field equations

Our interest in this work is to simulate the nonlinear wave-propagation phenomena that occur in the high-speed impact of munitions on targets. Such impacts result in rapid, even discontinuous loading of the material under deformation. The waves generated upon the impact loading may become propagating shock waves. Therefore, physically realistic weak solutions of the governing equations are sought. In the present work, the local Lax–Friedrichs Essentially Non-Oscillatory (LLF-ENO) schemes [6] are used for solving the conservation laws. In order to apply this method for integration of the equations, it has to be established first that the system of equations under consideration is indeed hyperbolic, i.e., that the eigenvalues of the Jacobian matrix for the system are all real. This was verified to be the case for the range of physical parameters of interest (material properties, velocities, etc.) by one of the authors [62]. Consider the particular case of the 1D system for uniaxial strain assuming plastic loading, with the governing equations written in conservative form:

$$\frac{\partial \rho}{\partial t} + \frac{\partial(\rho u)}{\partial x} = 0, \tag{21}$$

$$\frac{\partial(\rho u)}{\partial t} + \frac{\partial(\rho u^2 + p)}{\partial x} = \frac{\partial \tau_x}{\partial x}, \tag{22}$$

$$\frac{\partial E}{\partial t} + \frac{\partial u(E + p)}{\partial x} = \frac{\partial(u\tau_x)}{\partial x}, \tag{23}$$

$$\frac{\partial(\rho\bar{\varepsilon})}{\partial t} + \frac{\partial(\rho u\bar{\varepsilon})}{\partial x} = \left[\frac{1}{1 + \frac{\Sigma'}{3G}}\right]\frac{2\rho}{3}\left|\frac{\partial u}{\partial x}\right|, \tag{24}$$

$$\frac{\partial(\rho\tau_x)}{\partial t} + \frac{\partial(\rho u\tau_x)}{\partial x} = \left[1 - \frac{1}{1 + \frac{\Sigma'}{3G}}\right]\frac{4\rho}{3}G\frac{\partial u}{\partial x}. \tag{25}$$

Pressure is obtained from the equation of state. Note that the material strength terms have been placed in the source terms. The homogeneous part of the governing equations is the conservative form of the Euler hydrodynamic equations. The pressure (trace of the stress tensor) is included in the fluxes in Eqs. (22) and (23).

Writing this system in matrix form, i.e., as

$$\frac{\partial Q}{\partial t} + A\frac{\partial Q}{\partial x} = S(Q), \tag{26}$$

where the vector of independent variables

$$Q = \begin{bmatrix} \rho \\ \rho u \\ E \\ \rho\bar{\varepsilon} \\ \rho s_x \end{bmatrix} = \begin{bmatrix} q_1 \\ q_2 \\ q_3 \\ q_4 \\ q_5 \end{bmatrix}, \tag{27}$$

the flux vector is

$$F = \begin{bmatrix} \rho u \\ \rho u^2 + p \\ u(E+p) \\ \rho u\bar{\varepsilon} \\ \rho u\tau_x \end{bmatrix}, \tag{28}$$

and A is the Jacobian matrix

$$A = \frac{\partial F}{\partial Q}, \tag{29}$$

$S(Q)$ is the source term in Eq. (26). This quasilinear matrix form of the governing equations was used to explore the characteristic structure of the system. The Jacobian matrix A was obtained as in Eq. (29) for the homogeneous part of the above system, i.e., without the source terms $S(\cdot)$. Eigenvalues for the matrix were computed. The eigenvalues of the matrix, for the particular case of the Mie–Gruneison equation of state for pressure, are:

$$\lambda_1 = \lambda_2 = \lambda_3 = u, \tag{30a}$$

$$\lambda_4 = u - c, \tag{30b}$$

$$\lambda_5 = u + c, \tag{30c}$$

where the sound speed c is obtained from

$$c^2 = \frac{\rho_0\Gamma_0}{\rho^2}p + \rho_0^2 c_0^2 \frac{\rho + (s-\Gamma_0)(\rho-\rho_0)}{[\rho - s(\rho-\rho_0)]^3}. \tag{31}$$

These eigenvalues were found to be real for the range of parameters, i.e., material properties and impact velocities, of interest in this work. The above wave speed can also be obtained for a general e.o.s. of the form $p = p(\rho, e)$ as provided by Glaister [59] for the Euler equations, i.e.,

$$c^2 = \frac{p\left(\frac{\partial p}{\partial e}\right)_\rho}{\rho^2} + \left(\frac{\partial p}{\partial \rho}\right)_e \tag{32}$$

Note that the eigenvalues in this work are obtained by taking the plastic deformation terms on the right-hand side of the equations and treating them as source terms in the governing equations. This is justified on two grounds: (1) the elastic wave speeds are much higher than the plastic wave speeds and thus provide an upper bound on the propagation of the waves in the material, and (2) in the present work we are interested in impacts at high speeds and large deformations. In such cases the pressure forces arising from compression of the material are much larger than the deviatoric (strength) terms. Thus, the strength terms are treated as sources in the conservation law equations. The full analysis of the eigenvalues including elastic–plastic deformations has been presented by Trangenstein and Colella [63] and Miller and Colella [40].

5.1. LLF-ENO discretization of the hyperbolic conservation laws

To solve the hyperbolic system of equations in one- and two-dimensions, the ENO shock-capturing scheme [4,5] was used. The scheme was modified to treat the presence of the moving embedded material–material and material–void boundaries. The Convex ENO scheme due to Liu and Osher [6] was implemented, to enable the oscillation-free solution of the two-dimensional equations without field-by-field decomposition in the presence of large gradients. The discretization proceeds as described below.

Consider the governing equation for one-dimensional transport

$$\frac{\partial \vec{Q}}{\partial t} + \frac{\partial F(\vec{Q})}{\partial x} = S(\vec{Q}). \tag{33}$$

Let

$$\frac{\partial \vec{Q}}{\partial t} = L(\vec{Q}), \tag{34}$$

where

$$L(\vec{Q}) = -\frac{F_e - F_w}{x_e - x_w} + D(\vec{Q}), \tag{35}$$

F_e and F_w are the fluxes at the east and west faces shown, and x_e and x_w are the locations of the east and west faces, respectively, as shown in Fig. 4. D is an appropriate discrete operator for the source terms. In the current work, the source terms are discretized using a second-order central difference scheme. This was found to be robust for the calculations performed. However, it may be necessary in future work to develop a more sophisticated differencing procedure for the source terms as well.

The three-step third-order in time Runge–Kutta scheme is used in this work and takes the form [4,5]

$$\begin{aligned}
\vec{Q}^{(1)} &= \vec{Q}^{(n)} + \Delta t L(\vec{Q}^{(n)}),\\
\vec{Q}^{(2)} &= \frac{1}{4}(\vec{Q}^{(1)} + 3\vec{Q}^{(n)}) + \frac{1}{4}\Delta t L(\vec{Q}^{(1)}),\\
\vec{Q}^{(n+1)} &= \frac{1}{3}(2\vec{Q}^{(2)} + \vec{Q}^{(n)}) + \frac{2}{3}\Delta t L(\vec{Q}^{(2)}).
\end{aligned} \tag{36}$$

The spatial order of accuracy of the ENO formulation used to solve Eq. (33) is determined by the interpolation practices used to evaluate the fluxes at the faces e and w, i.e., in obtaining F_e and F_w in Eq. (35). A non-uniform mesh implementation of the fluxes in the ENO formulation is used here due to the presence of immersed boundaries, as illustrated in Fig. 4(b). With particular reference to cell j, in the 1D case the interface can lie anywhere between x_j and x_{j+1}. The two materials are treated separately in the sharp interface formulation and the flux F_e is evaluated at a location $(x_j + x_{int})/2$ when an immersed interface is present between nodes j and $j+1$. Thus, the spacing for cell j is different for the e and w faces. The flux evaluations for the ENO formulation come from derivatives of an interpolating function $H(x)$ as follows:

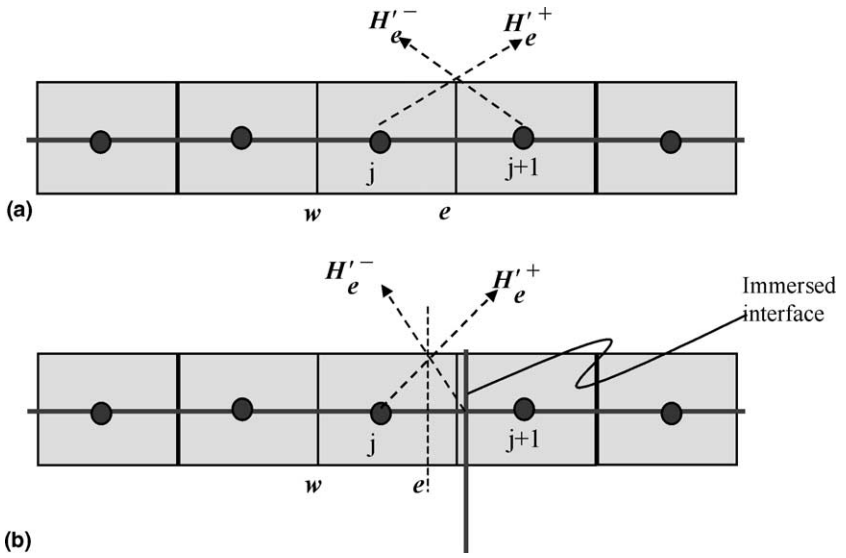

Fig. 4. (a) Illustration of grid point and grid face definitions for discretization of governing equations. H'^{+} and H'^{-} are derivatives of the interpolating function evaluated from the left and right stencils, respectively. (b) Grid point and grid face definitions for evaluation of fluxes in the presence of an immersed boundary.

$$F_{\mathrm{e}} = \frac{\mathrm{d}}{\mathrm{d}x}[H(x)]_{x=x_{\mathrm{e}}}. \tag{37}$$

The derivatives are evaluated from divided differences and the flux evaluation is performed as follows:

$$F_{\mathrm{e}} = F_{\mathrm{e}}^{+} + F_{\mathrm{e}}^{-} = H'^{+}(x_{\mathrm{e}}) + H'^{-}(x_{\mathrm{w}}). \tag{38}$$

The superscripts (+) and (−) indicate the positive and negative direction fluxes at the face e under consideration as illustrated in Fig. 4. The derivatives H' are obtained as explained below. Consider the interpolating function $H(x)$. In terms of the divided differences this function can be written as

$$H(x) = H[x_0] + H[x_0, x_1](x - x_0) + H[x_0, x_1, x_2](x - x_0)(x - x_1) + \mathrm{O}(h^3). \tag{39}$$

This interpolating polynomial can be carried to higher orders. We will restrict attention here to developing an $\mathrm{O}(h^2)$ flux approximation, although higher-order implementations have been used in calculations shown later. In the above $H[\cdot,\cdot]$ symbolizes the first divided difference and the higher-order divided differences are obtained successively. The Essentially Non-Oscillatory (ENO) schemes [4,5] are derived from a suitable choice of the stencil locations $(x_0, x_1, x_2, \ldots)$ from which the interpolating function is constructed.

Note that due to the possibility of a non-uniform stencil at the interfacial nodes, we have written the computer code in a general setting, as in Eq. (39). Then the ENO flux calculations proceed as usual. Since a uniform Cartesian grid is used, at non-interfacial nodes these fluxes are no different from standard ENO implementation on uniform grids. For example, looking at Fig. 5(a) it is clear that there is only one stencil possible for the first divided difference for control point location j, while there are two candidate stencils (shown in Figs. 5(b) and (c)) for the second divided difference, as represented by the forward and backward differences in the divided difference table. The ENO scheme and its variants derive their essentially non-oscillatory property from the choice of stencils adopted. The original ENO scheme [3–5] chooses the "smoothest" stencil, i.e., the lesser of the two values for the divided differences obtained from the stencils in Figs. 5(b) and (c). Weighted ENO schemes [64] devise appropriate weights for each candidate divided

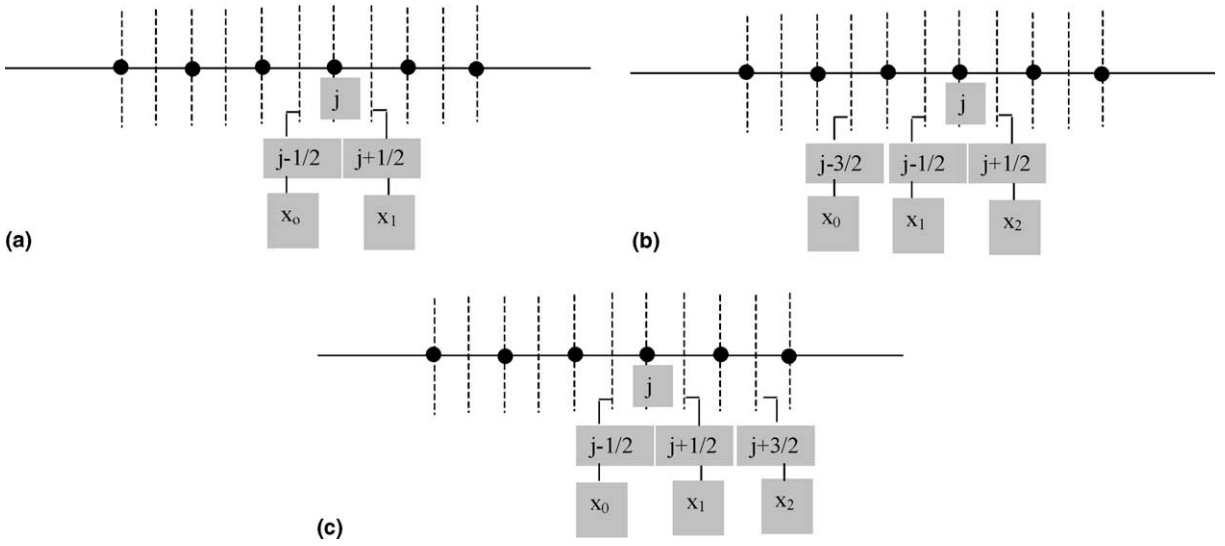

Fig. 5. Illustration of stencils used for obtaining the derivative $H'^{(+)}$ at face $x_{j+\frac{1}{2}}$: (a) first-order stencil, (b) second-order stencil for $H'^{(2a)+}$, (c) second-order stencil for $H'^{(2b)+}$.

difference and then evaluate the weighted divided difference. The present formulation is based on the Convex ENO scheme proposed by Liu and Osher [6] and chooses the divided difference value "closest" to the previous (here the first-) order flux chosen. It is this adaptive stencil choice procedure that enables the Lax–Friedrichs-based ENO scheme to obtain non-oscillatory solutions in the vicinity of the shock, while avoiding smearing of solutions in the smooth regions of the flowfield. The scheme reduces to low-order automatically at discontinuities, while maintaining higher order in smooth regions. Now, the first divided difference is obtained as follows:

$$H'^{+}(x_e) = H^{+}\left[x_{j-\frac{1}{2}}, x_e\right] = \frac{1}{2}\left(f(q[x_j]) + \alpha_{j+\frac{1}{2}} q[x_j]\right) \tag{40a}$$

and

$$H'^{-}(x_e) = H^{-}\left[x_e, x_{j+\frac{3}{2}}\right] = \frac{1}{2}\left(f(q[x_{j+1}]) - \alpha_{j+\frac{1}{2}} q[x_{j+1}]\right), \tag{40b}$$

where $\alpha_{j+(1/2)}$ is the characteristic speed evaluated at the cell face location $x_{j+(1/2)}$. This is evaluated as the maximum eigenvalue of the set in Eqs. (30a)–(30c) at the cell face.

Note that in general:

$$H^{+}[x_0, x_1]|_{x=x_1} = \frac{1}{2}(f(q(\bar{x})) + \alpha(x_1) q(\bar{x})), \tag{41a}$$

$$H^{-}[x_0, x_1]|_{x=x_0} = \frac{1}{2}(f(q(\bar{x})) - \alpha(x_0) q(\bar{x})), \tag{41b}$$

where

$$\bar{x} = \frac{(x_0 + x_1)}{2}. \tag{42}$$

These of course apply to nodes away from the immersed boundary such as $j-1$ in Fig. 4(b). For points that are adjacent to the immersed interface such as j in Fig. 4(b), the flux evaluations need to be modified. Here, the east face is not the grid cell face but is located at $\frac{1}{2}(x_j + x_{\text{int}})$, where x_{int} is the location of the interface. Therefore, for point j:

$$H'^{+}(x_e) = H\left[x_{j-\frac{1}{2}}, x_{\text{int}}\right] = \frac{1}{2}\left(f(q[x_j]) + \alpha_{j+\frac{1}{2}} q[x_j]\right), \tag{43a}$$

$$H'^{-}(x_e) = H[x_e, x_{\text{int}}] = \frac{1}{2}\left(f(q_{\text{int}}) - \alpha_{j+\frac{1}{2}} q_{\text{int}}\right), \tag{43b}$$

where q_{int} is the interfacial value of the convected scalar variable q. This value needs to be obtained from appropriate boundary conditions applied at the interface. This type of interfacial flux treatment of course reduces the order of accuracy at the immersed boundaries by one order. However, the high-order scheme is retained in the bulk of the computational domain. Similar considerations apply in the Ghost Fluid Method due to Fedkiw and coworkers [52,53] for multifluid interactions.

The first-order flux at the interface is then obtained using Eqs. (40a) and (40b), or Eqs. (43a) and (43b) if node j adjoins the interface. In order to determine the second-order divided difference, the following steps are taken.

As a matter of notation we denote the first-order flux at cell face located at $x_{j+\frac{1}{2}}$ as

$$\tilde{f}(j, j, +1) = H^{+}\left[x_{j-\frac{1}{2}}, x_{j+\frac{1}{2}}\right] = \frac{1}{2}\left(f(q(x_j)) + \alpha_{j+\frac{1}{2}} q[x_j]\right), \tag{44}$$

where the notation for the flux at the face in terms of $\tilde{f}(j1, j2, \pm 1)$ indicates that the flux is computed for the face of cell $j2$ using values at control point $j1$. The ± 1 indicates the direction of flux computed. Therefore, following this notation, the flux in the negative direction at cell face located at $x_{j+\frac{1}{2}}$ is given by

$$\tilde{f}(j+1, j, -1) = H^{-}\left[x_{j+\frac{1}{2}}, x_{j+\frac{3}{2}}\right] = \frac{1}{2}\left(f(q(x_{j+1})) - \alpha_{j+\frac{1}{2}} q[x_{j+1}]\right). \tag{45}$$

The candidate second-order derivatives of the interpolating function $H(x)$ at cell face $x_{j+\frac{1}{2}}$ are

$$\begin{aligned} H'^{(2a)+}\left(x_{j+\frac{1}{2}}\right) = {} & H^{+}\left[x_{j-\frac{3}{2}}, x_{j-\frac{1}{2}}\right] + \frac{\left(x_{j-\frac{3}{2}} + x_{j-\frac{1}{2}} - 2x_{j+\frac{1}{2}}\right)}{\left(x_{j+\frac{1}{2}} - x_{j-\frac{3}{2}}\right)} H^{+}\left[x_{j-\frac{3}{2}}, x_{j-\frac{1}{2}}\right] \\ & + \frac{\left(2x_{j+\frac{1}{2}} - x_{j-\frac{3}{2}} - x_{j-\frac{1}{2}}\right)}{\left(x_{j+\frac{1}{2}} - x_{j-\frac{3}{2}}\right)} H^{+}\left[x_{j-\frac{1}{2}}, x_{j+\frac{1}{2}}\right], \end{aligned} \tag{46}$$

which can be written based on the notation in Eqs. (43a), (43b) and (44) as

$$H'^{(2a)+}\left(x_{j+\frac{1}{2}}\right) = \tilde{f}(j-1, j, +1) + A^{(2a)+}\tilde{f}(j-1, j, +1) + B^{(2a)+}\tilde{f}(j, j, +1), \tag{47}$$

where A and B are grid-dependent factors determined by the locations of the stencil points chosen. Similarly, the other candidate second-order fluxes can be written as

$$H'^{(2b)+}\left(x_{j+\frac{1}{2}}\right) = \tilde{f}(j, j, +1) + A^{(2b)+}\tilde{f}(j, j, +1) + B^{(2b)+}\tilde{f}(j+1, j, +1), \tag{48}$$

$$H'^{(2a)-}\left(x_{j+\frac{1}{2}}\right) = \tilde{f}(j, j, -1) + A^{(2a)-}\tilde{f}(j, j, -1) + B^{(2a)-}\tilde{f}(j+1, j, -1), \tag{49}$$

$$H'^{(2b)-}\left(x_{j+\frac{1}{2}}\right) = \tilde{f}(j+1,j,-1) + A^{(2b)-}\tilde{f}(j+1,j,-1) + B^{(2b)-}\tilde{f}(j+2,j,-1). \tag{50}$$

Similar expressions for the third- and higher-order derivatives can be obtained. Therefore, for the second-order fluxes at the face $j+1/2$ there are two candidates each for the (+) and (−) direction contributions.

In the presence of immersed boundaries the discretization in the cells adjoining the interface only will need to be modified in two ways:

1. The interface boundary conditions will appear in the flux contributions from the interface side as in Eqs. (43a), (43b).
2. The stencil choices possible at such cells will be limited in the direction in which the interface lies. For example, with reference to Fig. 5, for cell j there will be one first-order stencil in each direction as for the interior cells. However, for interfacial cell j, there can be only one choice of second-order flux for the estimation of H'^{-}, i.e., we will only have $H'^{(2a)-}$, with $\tilde{f}(j+1,j,-1)$ replaced by $\tilde{f}(\text{int},j,-1)$ and suitable modification of the weights $A^{(2a)-}$ and $B^{(2a)-}$ because instead of extracting values from the node at x_{j+1}, they would be supplied at the interface location x_{int}. Also, for point j, for the H'^{+} contribution, while $H'^{(2a)+}$ will remain unchanged, $H'^{(2b)+}$ will be changed by replacing q_{j+1} by q_{int} and x_{j+1} by x_{int}.

The above considerations are no different in fact from that at the cell immediately in the interior of the domain boundary. Therefore, the immersed boundary treatment for evaluating fluxes is no different from that for domain boundary cells. Apart from these considerations the fluxes for the cell j adjoining the immersed boundary are constructed using Eqs. (38)–(40b) except that the values of q_{int}, i.e., boundary conditions on the immersed interface need to be used instead of the grid point q_j values in Eqs. (43a), (43b) and (47)–(50). It is not readily apparent how to compute the boundary values for all the dependent variables in the particular physical problem being computed. Some physically based boundary conditions can be imposed based on the physics of the impact phenomena. However, some of the physical quantities will require numerical boundary conditions as in other systems of PDEs. The boundary conditions chosen and the rationale for the choice are explained in the following sections. It is noted that in 2D the evaluation of fluxes is performed independently in the x- and y-directions using the ENO scheme separately for the field in each direction. The modifications for the flux evaluation in the presence of the immersed boundary follow for 2D in the same manner as in 1D.

6. Boundary and initial conditions

To evaluate the fluxes in the discrete form, Eq. (35), interfacial boundary conditions are required at marker locations on the interface. As can be seen in Fig. 6, an interfacial marker in the material–material region can have an immediate neighbor in the material–void region of the interface. Therefore, at each

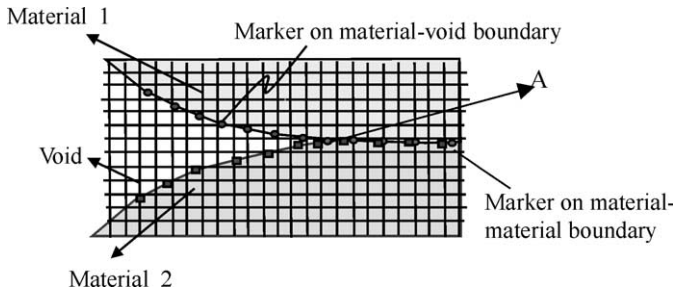

Fig. 6. Illustration of marker location and the type of boundary condition at the different interface regions.

instant of the interface deformation, the interface markers have to be classified as material–material (MM) or material–void (MV) markers and the appropriate b.c.'s obtained there. This is done by interrogating the grid nodes surrounding each marker point and determining the materials present at these nodes. If all of these surrounding nodes lie either in the material enclosed by the interface to which that marker point belongs or in the void, the marker is classified as a MV point. On the contrary, if any of the surrounding grid nodes lies in a different material (which is not a void) then the marker is classified as an MM point. Thus, it is possible for two immediate interfacial marker neighbors to have entirely different b.c.'s (i.e. MM or MV) imposed on them.

6.1. Type 1: material–material interface

Boundary conditions in the material–material case are developed based on the physically required conditions of continuous material point velocities at the interface for the two materials and the continuity of stress and temperature. These can be stated as (+ and − superscripts indicating the two sides of the contact surface)

$$u^+ = u^- = u_{\text{int}}, \tag{51a}$$

$$v^+ = v^- = v_{\text{int}}, \tag{51b}$$

$$\sigma_{xx}^+ = \sigma_{xx}^- = (\sigma_{xx})_{\text{int}}, \tag{51c}$$

$$\sigma_{yy}^+ = \sigma_{yy}^- = (\sigma_{xy})_{\text{int}}, \tag{51d}$$

$$\sigma_{xy}^+ = \sigma_{xy}^- = (\sigma_{xy})_{\text{int}}, \tag{51e}$$

$$T^+ = T^- = T_{\text{int}}. \tag{51f}$$

The interface values are obtained by bilinear interpolation from the surrounding mesh points. Assuming the two impacting bodies are made of the same material, this last condition amounts to

$$E^+ = E^- = E_{\text{int}}. \tag{51g}$$

Note that for the impact of a deformable material with a rigid one, as studied in this work, the velocity of the material–material interface is set to zero. Along with the equation of state for the pressure these constitute seven physically imposed conditions at the interface for the nine independent variables $(\rho, u, v, p, E, \tau_{xx}, \tau_{yy}, \tau_{xy}, \varepsilon)$. This necessitates numerical boundary conditions to be developed for the remaining dependent variables.

For the material–material contact situation shown in Fig. 6, the boundary conditions are imposed on the interfacial markers shown on the interface by the filled circles. The following numerical boundary conditions are applied:

$$\rho^{\pm} = \Xi(\rho_h), \tag{52a}$$

$$E^{\pm} = \Xi(E_h), \tag{52b}$$

$$\bar{\varepsilon}^{\pm} = \Xi(\bar{\varepsilon}_h), \tag{52c}$$

$$p^{\pm} = \mathrm{eos}\left(\rho^{\pm}, (\rho u^2)^{\pm}, (\rho v^2)^{\pm}, E^{\pm}\right), \tag{52d}$$

$$u^{\pm} = I(u_h), \tag{52e}$$

$$v^{\pm} = I(v_h), \tag{52f}$$

$$(\tau_{xx} + p)^{\pm} = I((\tau_{xx} + p)_h), \tag{52g}$$

$$(\tau_{yy} + p)^{\pm} = I((\tau_{yy} + p)_h), \tag{52h}$$

$$(\tau_{xy})^{\pm} = I((\tau_{xy})_h). \tag{52i}$$

The subscript h indicates values on the grid while superscripts $\pm$ indicate values on the (+) and (−) sides of the interface. In the above the operators Ξ and I are the extrapolation and interpolation operators, respectively. Note that the first-order extrapolation from within each material, in a direction normal to the interface, is employed and values on both sides of the interface are stored for each marker. A bilinear interpolation operator is used to estimate the variables that are continuous across the interface. When the interface conditions are obtained at impact boundaries "overheating" of the material can result as pointed out by Glaister [59]. The problem arises due to the collision of the impinging shock on a solid wall and the reflected shock coming off a solid wall [46]. The overshoots in the density and temperature are numerical artifacts that arise due to the unphysical dissipation inherent in the numerical schemes and the inability of the Euler equations to conduct heat away from the overheated region into the wall thus causing a buildup of temperature [65]. Pressure and velocity appear to equilibrate quickly but internal energy (temperature) does not and the use of the e.o.s. renders the density value inaccurate also. This problem will be shown to exist in both Eulerian and Lagrangian computations of impact. A fix for this problem has been suggested by Fedkiw et al. [58] for the case of gases and other materials. In the present computations with solids this fix has not been applied since further examination of this condition is required to determine its suitability to materials with strength, since the pressure in the present case is also related to the stresses in the material.

6.2. Type 2: material–void interface

For a material–void interface, the physically imposed conditions on the interface are that the surface tractions be negligible. Therefore

$$\vec{n} \cdot (-pI + T) = 0, \tag{53}$$

where I is the unit tensor and T is the deviatoric stress tensor. In the 1D case the zero traction condition reduces to

$$\sigma_x^{\pm} = (\tau_x - p)^{\pm} = 0. \tag{54}$$

This condition is easily applied at the material–void interface in 1D for the independent variable τ_x at the interface, since the pressure is given by the equation of state.

In the two-dimensional case, implementation of this boundary condition requires care. To apply the zero-traction condition, we first rotate the stress tensor as follows. Let

$$\hat{\sigma} = A^{\mathrm{T}} \sigma A, \tag{55}$$

where

$$\hat{\sigma} = \begin{bmatrix} \sigma_{nn} & \sigma_{nt} \\ \sigma_{tn} & \sigma_{tt} \end{bmatrix} \quad \text{and} \quad A = \begin{bmatrix} n_x & -n_y \\ n_y & n_x \end{bmatrix}$$

are the rotated stress and orientation matrices due to the transformation from x–y to t–n coordinates, the latter coordinates having axes oriented along the tangent and normal to the interface. Following expansion of Eq. (55), writing in terms of the deviatoric components τ_{ij}, and setting the surface tractions to zero at all the marker points, i.e., σ_{nn} and $\sigma_{nt} = 0$, we get, after some simplification

$$(\sigma_{tt})n_x^2 + p = \tau_{yy}, \tag{56}$$

$$(\sigma_{tt})n_y^2 + p = \tau_{xx}, \tag{57}$$

$$-(\sigma_{tt})n_x n_y = \tau_{xy}. \tag{58}$$

Along with the e.o.s. for pressure, which applies at the interface on the material side, these equations provide four equations for the five unknowns (σ_{tt}, τ_{xx}, τ_{xy}, τ_{yy}, and p) at the interface. To solve the above, we obtain the stress σ_{tt} by extrapolation from the interior of the material. It is, therefore, implicit in this boundary condition that boundary layers of the normal stress component aligned tangent to the free surface σ_{tt} are avoided at the material–void interface. Numerical b.c.'s at this free surface are required for the other flow variables and these are devised based on extensions from the 1D case and by experimentation to determine that the b.c.'s imposed do not lead to development of unphysical features in the flowfield. The b.c.'s imposed on the material (−ve) side of the interface are as follows, with the normal pointing from the material to the void by convention:

$$\rho^- = \Xi(\rho_h), \tag{59a}$$

$$E^- = \Xi(E_h), \tag{59b}$$

$$\bar{\varepsilon}^- = \Xi(\bar{\varepsilon}_h), \tag{59c}$$

$$u^- = \Xi(u_h), \tag{59d}$$

$$v^- = \Xi(v_h), \tag{59e}$$

$$p^- = \mathrm{eos}(\rho^-, (\rho u^2)^-, (\rho v^2)^-, E^-). \tag{59f}$$

The deviatoric stresses are then obtained from Eqs. (56) to (58). Note that no boundary conditions are required on the void side of the interface.

In all of the above, we have employed linear interpolation and extrapolation operators to obtain the numerical boundary conditions. The subscripts h in the operators indicate that interpolation and extrapolation to the interface are performed using values at the computational nodes on the Cartesian mesh.

7. One-dimensional (uniaxial strain) calculations

The ENO scheme described above has been applied to various one-dimensional problems to verify the ability of the scheme to capture discontinuities in the system of interest in this paper, which is distinguished by the following features:

1. The Mie–Gruneisen equation of state for pressure.
2. Material deformation and flow with elasto-plastic constitutive model.
3. Multiple immersed boundaries with different boundary conditions.

In this section we apply the ENO scheme to study its accuracy and robustness properties and we obtain insights into the performance of the scheme for the class of problems typical of multimaterial impact. Further, we compare the results of Eulerian calculations of the wave dynamics with Lagrangian calculations in 1D. Lagrangian calculations are performed using a standard second-order accurate Lagrangian code with artificial viscosity to handle large gradients. Lagrangian solvers are commonly employed in hydrocodes [9] and it is useful to compare the performance of the present Eulerian method with such methods for problems involving elasto-plastic deformation.

We first present results for a Riemann problem in air for hydrodynamic shocks upon impact and in solids for elastic–plastic shocks due to impact. These test cases demonstrate that the current Eulerian ENO-based framework performs accurate tracking of the various types of waves in elasto-plastic impact and the capability of the present method to calculate the dynamics of materials with strength is similar to that for the simple Euler hydrodynamic system.

7.1. Sod problem – ideal gas

The Sod problem is an often-used test case for numerical schemes. It is defined by the initial conditions

$$\mathbf{q}(x,0) = \begin{cases} \mathbf{q}_{\mathrm{L}}, & x < 0, \\ \mathbf{q}_{\mathrm{R}}, & x > 0, \end{cases} \tag{60}$$

where $\mathbf{q}_{\mathrm{L}} = (\rho_{\mathrm{L}}, v_{\mathrm{L}}, p_{\mathrm{L}}) = (\rho_0, 0, p_0)$ and $\mathbf{q}_{\mathrm{R}} = (\rho_{\mathrm{R}}, v_{\mathrm{R}}, p_{\mathrm{R}}) = (0.125\rho_0, 0, 0.1p_0)$, L and R implying the states to the left and right of the initial discontinuity. The material for the Sod problem in Fig. 7 is an ideal gas with ratio of specific heats $\Gamma = 1.4$. Figs. 7(a)–(d) compare the computed results to the exact solution of the Sod problem and to the solution from a Lagrangian method. The initial mesh for the Lagrangian calculation was identical to the Eulerian mesh. The Eulerian and Lagrangian calculations capture the shock and expansion fan with comparable accuracy, with the Lagrangian slightly overshooting at the tail of the expansion. The contact discontinuity, visible in the density and internal energy plots, is quite different in the Eulerian and Lagrangian results. The Lagrangian solver has no mechanism to diffuse the jump in density or internal energy, and captures the contact discontinuity in a single element width. The Eulerian solver must convect the discontinuity through the fixed mesh, and introduces dissipation that smears the contact. However, the Lagrangian result has a significant overshoot of internal energy (due to overheating) at the contact discontinuity, while the essentially non-oscillatory behavior of the Eulerian solver is maintained. The ENO scheme is known to smear contact discontinuities and remedies have been suggested to correct this limitation [58] but are not applied in this study.

7.2. Impact on elasto-plastic material

Calculations of one-dimensional motion have been performed to verify the ability of the method to correctly capture discontinuities in an elastic–plastic medium. One-dimensional motion, or uniaxial strain, is a reasonable model of material response in the neighborhood of a planar shock. For a material described by a Mie–Gruneisen equation of state and perfectly plastic response, it is possible to determine the exact solution to the uniaxial strain equations under the application of a step velocity change at the boundary. The exact response has the classical structure of a fast wave called the elastic precursor followed by a stronger wave that induces plastic deformation. Both waves are mathematically predicted to be sharp discontinuities for the material model used here. Since the exact solution for an

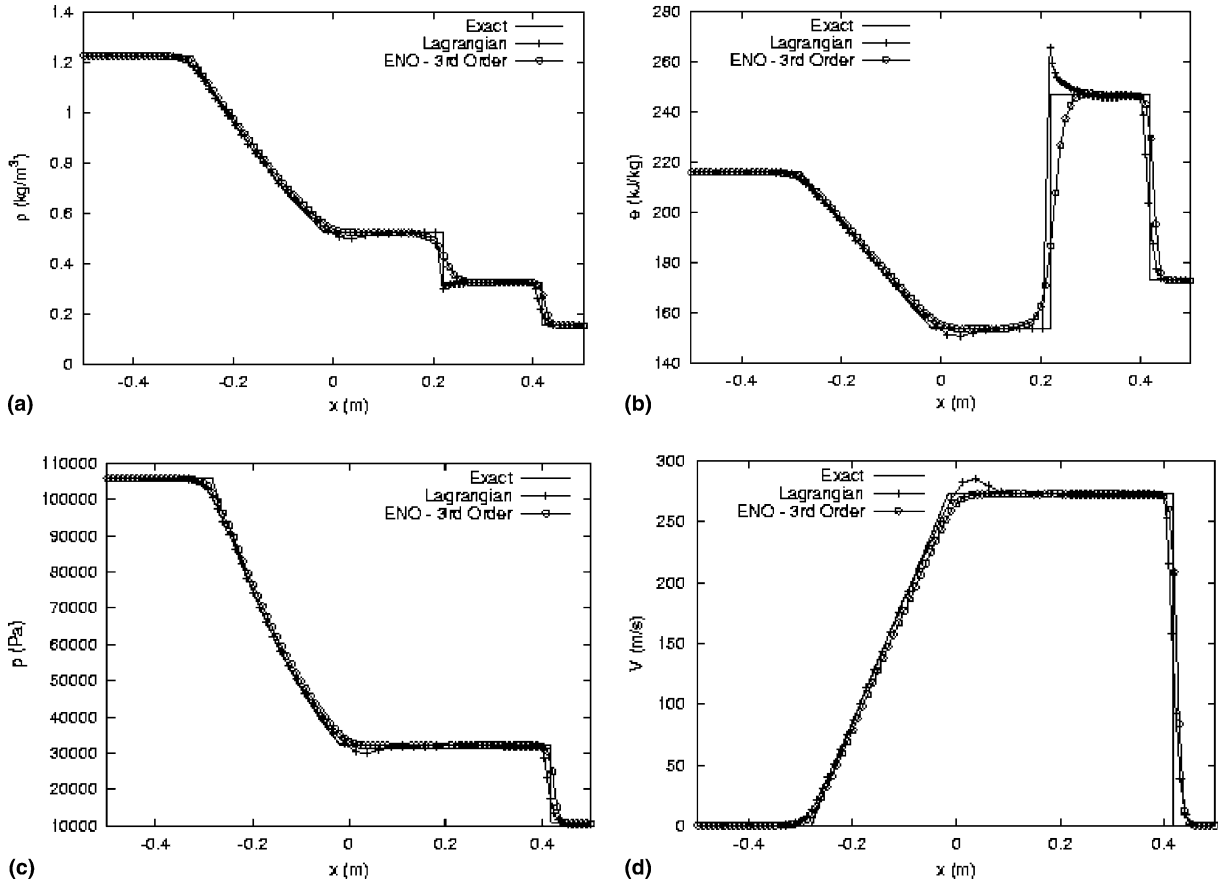

Fig. 7. Sod problem for an ideal gas (air). Euler equations are solved. Exact solutions are shown along with the results for a second-order accurate Lagrangian method and the third-order ENO Eulerian method: (a) density, (b) internal energy, (c) pressure, (d) velocity.

elastic–plastic shock system accounting for the nonlinear equation of state is not often given, it will be briefly described below. The initial state of the material is taken such that pressure and particle velocity are zero, and the internal energy is given a value corresponding to room temperature. Conditions after the passage of the elastic precursor with wave speed U_{se} are denoted with the superscript Y, corresponding to the ''yield'' conditions, often called the Hugoniot elastic limit conditions. After passage of the stronger inelastic wave, with wave speed U_s, the final conditions are denoted by subscript 2. Some property of the material at the final state is required to close the system of equations, and we assume that the final particle velocity, v_2, is known.

Below the yield stress, the rate of change of deviatoric stress is given by

$$\tau_x = \frac{4}{3} G \frac{\partial v}{\partial x}, \tag{61}$$

which when integrated for uniaxial motion gives

$$\tau_x = \frac{4}{3} G \ln \frac{\rho_0}{\rho}. \tag{62}$$

This will hold until the deviatoric stress reaches the yield point, which is related to the yield stress in a uniaxial stress test, Y, by

$$\tau_x^Y = -\frac{2}{3}Y, \tag{63}$$

where the negative stress indicates compression.

The density at the point of compressive yielding is

$$\rho^Y = \rho_0 \exp\left(\frac{Y}{2G}\right). \tag{64}$$

From shock jump relations, the speed of propagation of the elastic wave U_{se} is related to the total stress at the yield point $\sigma^Y = s_x^Y - p^Y$, by the slope of the Rayleigh line, giving

$$U_{se}^2 = \frac{\rho^Y \sigma^Y}{\rho_0(\rho_0 - \rho^Y)}. \tag{65}$$

The pressure at the yield point p^Y must be consistent with the equation of state relating pressure, density, and internal energy.

The internal energy jump across the elastic precursor is given by the Hugoniot equation

$$e^Y = \frac{1}{2\rho^Y \rho_0}\left(p^Y + \frac{2}{3}Y\right)(\rho^Y - \rho_0). \tag{66}$$

This is an implicit relation for e^Y because the pressure depends on internal energy via the equation of state. The Mie–Gruneisen equation of state, Eq. (5), can be written in the form

$$p(\rho, e) = p_r(\rho) + \rho\Gamma(e - e_r(\rho)). \tag{67}$$

Substituting this expression for p into the Hugoniot equation and solving for internal energy jump gives

$$e^Y = \frac{\left(p_r^Y - \rho^Y \Gamma^Y e_r^Y + \frac{2}{3}Y\right)(\rho^Y - \rho_0)}{2\rho_0\rho^Y - \rho^Y\Gamma^Y(\rho^Y - \rho_0)}, \tag{68}$$

where the superscript Y indicates that functions are evaluated at the yield point.

Now that the internal energy and density are known, the pressure, total stress, and wave speed can be obtained from previous relations. The particle velocity is given by

$$v^Y = \frac{\rho^Y - \rho_0}{\rho^Y} U_{se}. \tag{69}$$

The state of the material behind the plastic shock with speed U_s can be obtained from the shock jump relations written for a case with non-zero initial velocity and stress, namely:

$$\begin{aligned} p_2 &= p^Y + \rho^Y(U_s - v^Y)(v_2 - v^Y), \\ \rho_2 &= \rho^Y \frac{U_s - v^Y}{U_s - v_2}, \\ e_2 &= e^Y + \frac{1}{2\rho^Y\rho_2}\left(p^Y + p_2 - 2\tau_x^Y\right)(\rho_2 - \rho^Y). \end{aligned} \tag{70}$$

With the addition of the Mie–Gruneisen equation of state and assuming that v_2 is known, there are four equations that can be solved for the unknowns p_2, ρ_2, e_2, and U_s. The approach used here is to form the residual

$$r(U_s) = p_2(U_s) - p^{eos}(\rho_2(U_s), e_2(p_2(U_s), \rho_2(U_s))). \tag{71}$$

The root of the residual yields a value for U_s and the other values are easily obtained.

For the one-dimensional calculations performed here, the body extends from $x = -1$ to $x = 1$ m. Impact at the $x = 0$ surface is modeled by imposing a step change in initial velocity at $x = 0$. The Gruneisen equation of state parameters are $\Gamma = 2.0$, $c_0 = 3940$ m/s, $s = 1.49$, with initial density $\rho_0 = 8930$ kg/m^3, shear modulus $G = 45$ GPa, and yield stress $Y = 90$ MPa in uniaxial stress. The initial internal energy is 110,920 J/kg. The initial particle velocity is zero for $x > 0$ and is either 40 or 2000 m/s for $x < 0$. The 40 m/s material impacting the initially stationary material results in a 20 m/s final particle velocity, while the 2000 m/s results in a particle velocity of 1000 m/s behind the shock. The relatively small yield strength is negligible relative to the pressure developed in the 1000 m/s case, but is significant for the 20 m/s case. For this reason, both elastic–plastic and hydrodynamic calculations ($s_x \equiv 0$) were performed for the 20 m/s case, but only hydrodynamic results are presented for the 1000 m/s case. All calculations are compared with 'exact' values obtained from the formulas above and given in Table 1. It is interesting to note that the final state of the material after passing through a single hydrodynamic shock to reach a particle velocity of 20 m/s is not the same as the state after an elastic–plastic shock system. For example, the pressure is lower in the elastic–plastic case, but the total longitudinal stress is higher. The computed results described below appear to correctly capture the stress state in the material and the wave velocities given in Table 1 are also correctly obtained.

The 1000 m/s hydrodynamic results are shown in Figs. 8(a)–(d). The exact shock speed is 5430 m/s, the density is 10945.8 kg/m^3, and the internal energy jump is 0.5 MJ/kg. The final pressure is 48.49 GPa. The snapshot of the motion is 170 μs after impact, and the single shock wave has moved approximately 0.92 m. To better see the structure of the shock, the figures show a small region around the shock. The figures compare first-, second-, and third-order Eulerian results at a fixed mesh spacing of 0.01 m and a fixed Courant number of 0.6. Results are also shown for a uniaxial Lagrangian calculation for reference. The Lagrangian calculation is performed on a mesh with initial spacing of 0.01 m (same as the Eulerian mesh) and Courant number of 0.6. There is an evident sharpening of the shock as the order of the Eulerian solution is increased, with about 10 points in the first-order shock and five points in the third-order shock. All variables compare well with the exact solution away from the shock. The Lagrangian solution is comparable to the second-order Eulerian solution in terms of the solution gradient within the shock, but approaches the third-order Eulerian solution in terms of number of number of points within the shock. The Lagrangian solution has a more abrupt end of the shock, while the Eulerian solution rounds the beginning and end of the shock region. We investigate this behavior of the Eulerian solution further in a later section.

The 20 m/s hydrodynamic results are given in Figs. 9(a)–(d). The exact shock speed is 3969.8 m/s, significantly slower than the 1000 m/s impact case. The exact density is 8975.2 and the internal energy jump is only 200 J/kg. The pressure is 709 MPa. Once again, a comparison of Eulerian results of various orders of accuracy and a Lagrangian calculation are given at 170 μs after impact. For this case, the motion at the impacted boundary after 170 μs is hardly noticeable on the scale of the plots, and the shock has only

Table 1
Exact values for variables for shocks of different strengths used in the computations as calculated from Eqs. (66)–(75)

	Hydro, 1000 m/s	Hydro, 20 m/s	Elastic precursor, 20 m/s	Plastic shock, 20 m/s
Wave speed (km/s)	5.430	3.970	4.722	3.977
Particle velocity (m/s)	1000	20	4.720	20
Density (kg/m^3)	10946	8975.2	8938.9	8973.5
Internal energy jump (J/kg)	500 000	200	11.138	213.53
Pressure (MPa)	48 490	709.01	139.03	681.59
Deviatoric stress (MPa)	0	0	−60	−60
Total stress (MPa)	−48 490	−709.01	−199.03	−741.59

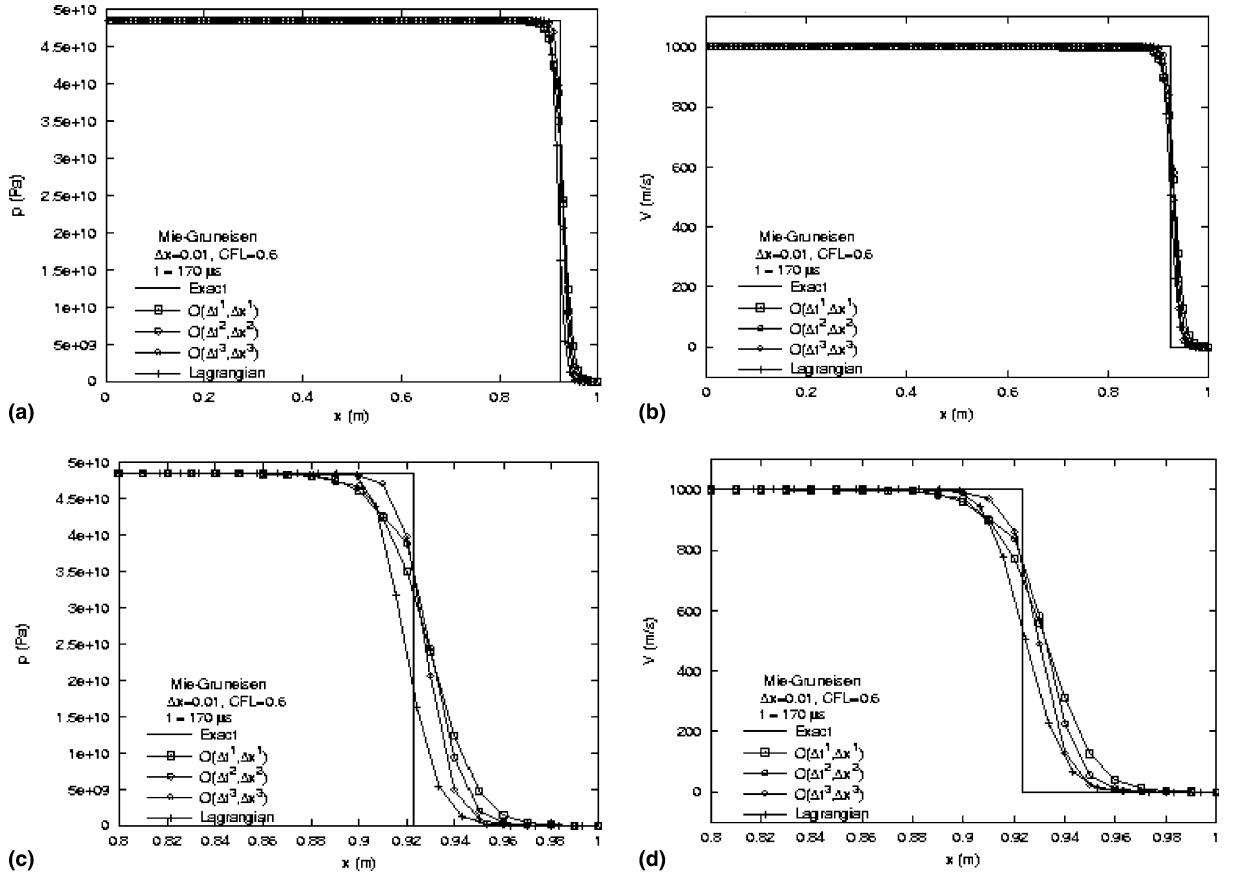

Fig. 8. Impact at 1000 m/s on a copper rod. Impact takes place at the left end. The Euler equations are solved with the Mie–Gruneisen equation of state: (a) pressure, (b) velocity, (c) close-up view of pressure profile in the vicinity of the shock, (d) close-up view of velocity in the vicinity of the shock.

progressed 0.67 of the length of the body. Note that the calculated profiles for this much weaker wave have roughly twice the points in the shock compared to the 1000 m/s calculations. The first-order solution has approximately 22 and the third-order solution has about 15. The Lagrangian solution is comparable to the second-order Eulerian in sharpness. The stronger shock's sharper solution is likely due to driving of the equation of state into a more nonlinear regime, with a larger difference in sound speed before and after the strong shock causing self-sharpening. The somewhat excessive dissipation of the shock by the ENO scheme for weak shocks also been observed by Fedkiw et al. [58]. The number of points in the shock has been shown in that work to depend on the shock strength and grid refinement applied to solve the weak shock problems. For stronger shocks, particularly in the gas dynamic system, as in the Sod problem above, the shock is captured within the traditional 2–3 grid points, independent of grid spacing. The 20 m/s results outside the neighborhood of the shock are excellent, except for internal energy. Internal energy loses accuracy at the location of the original velocity discontinuity, as shown in Fig. 9(a)). The relative error in the internal energy jump is greater for this case as compared to the 1000 m/s case, but the absolute error due to overheating in internal energy is much smaller. For the 20 m/s case, the error in density at the impact location is not noticeable. Both Eulerian and Lagrangian solutions overshoot the correct value and then slowly approach the correct value away from the contact region. The higher-order Eulerian calculations

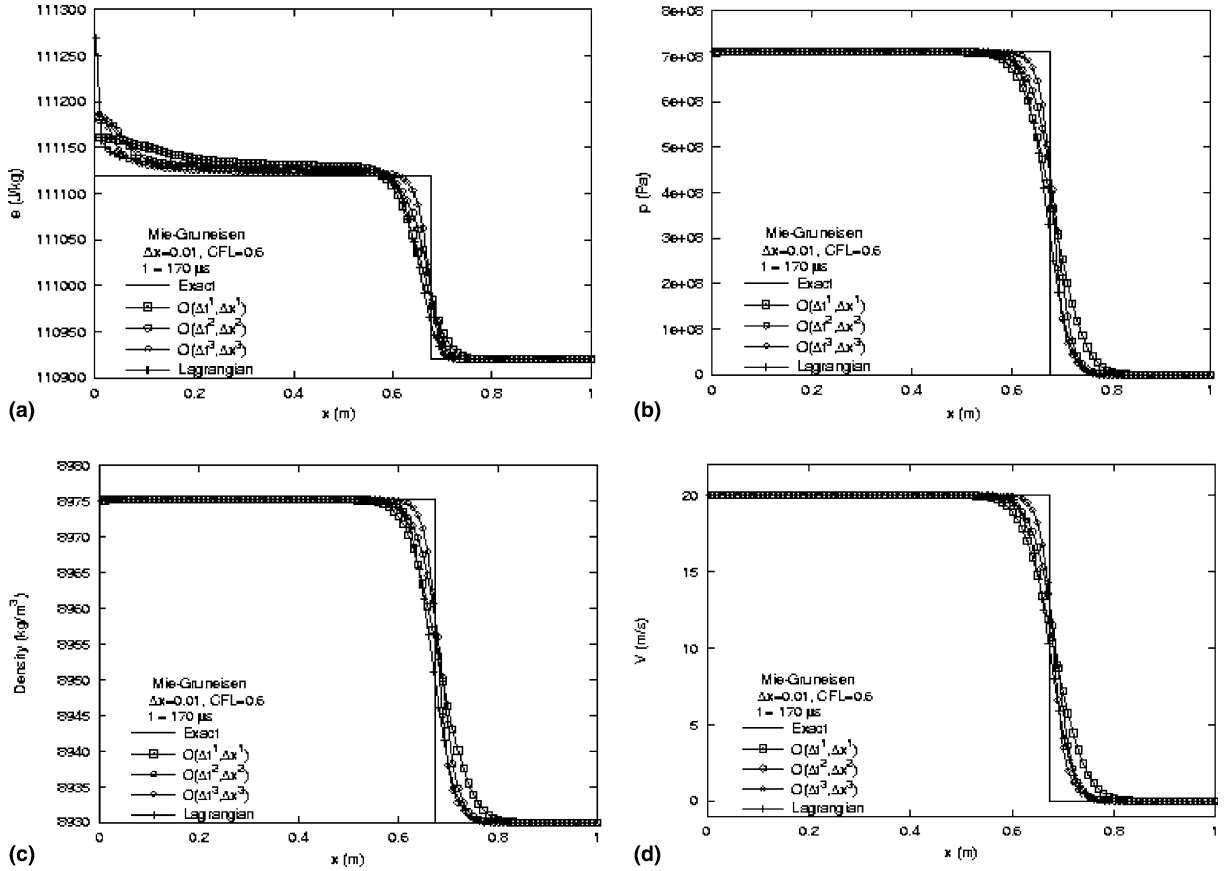

Fig. 9. Impact at 20 m/s on a metal rod (copper). Euler equations and the Mie–Gruneisen equation of state: (a) internale energy, (b) pressure, (c) density, (d) velocity.

overshoot more, but then approach the correct energy value more quickly than the low-order. The error in internal energy is accompanied by a relatively small error in density sufficient to compensate for the internal energy deviation and give the correct value of pressure. These overheating errors in energy and density can be corrected by applying an isobaric fix as proposed by Fedkiw et al. [58] or by adding a heat diffusion term at points adjacent to the left boundary as proposed by Donat and Marquina [65]. The applicability of these methods to materials with strength remains to be investigated.

The next set of figures, Figs. 10(a)–(f), show results for calculation of elastic–plastic flow with final particle velocity of 20 m/s at a Courant number of 0.6, a mesh spacing of 0.01, and at a time of 170 μs after impact. First-order, second-order, and third-order Eulerian results and a Lagrangian calculation are compared. The plots show the characteristic two-wave structure of the elastic–plastic response. The first-order calculations display so much dissipation that the elastic precursor and the inelastic shock are blended together. Both the second-order and the third-order results are significantly better. The number of points in the elastic and inelastic wave are each comparable to the hydrodynamic calculation at 20 m/s, but the proximity of the waves results in a smeared profile at this resolution. Notably, the dissipation of the shocks is not influenced by the material mode, i.e., the elastic and plastic wavefronts are captured in as many grid points as were the shocks in the Euler system. The velocity, pressure, density, and total stress match the exact results away from the shock. However, internal energy shows error at the impact location similar to

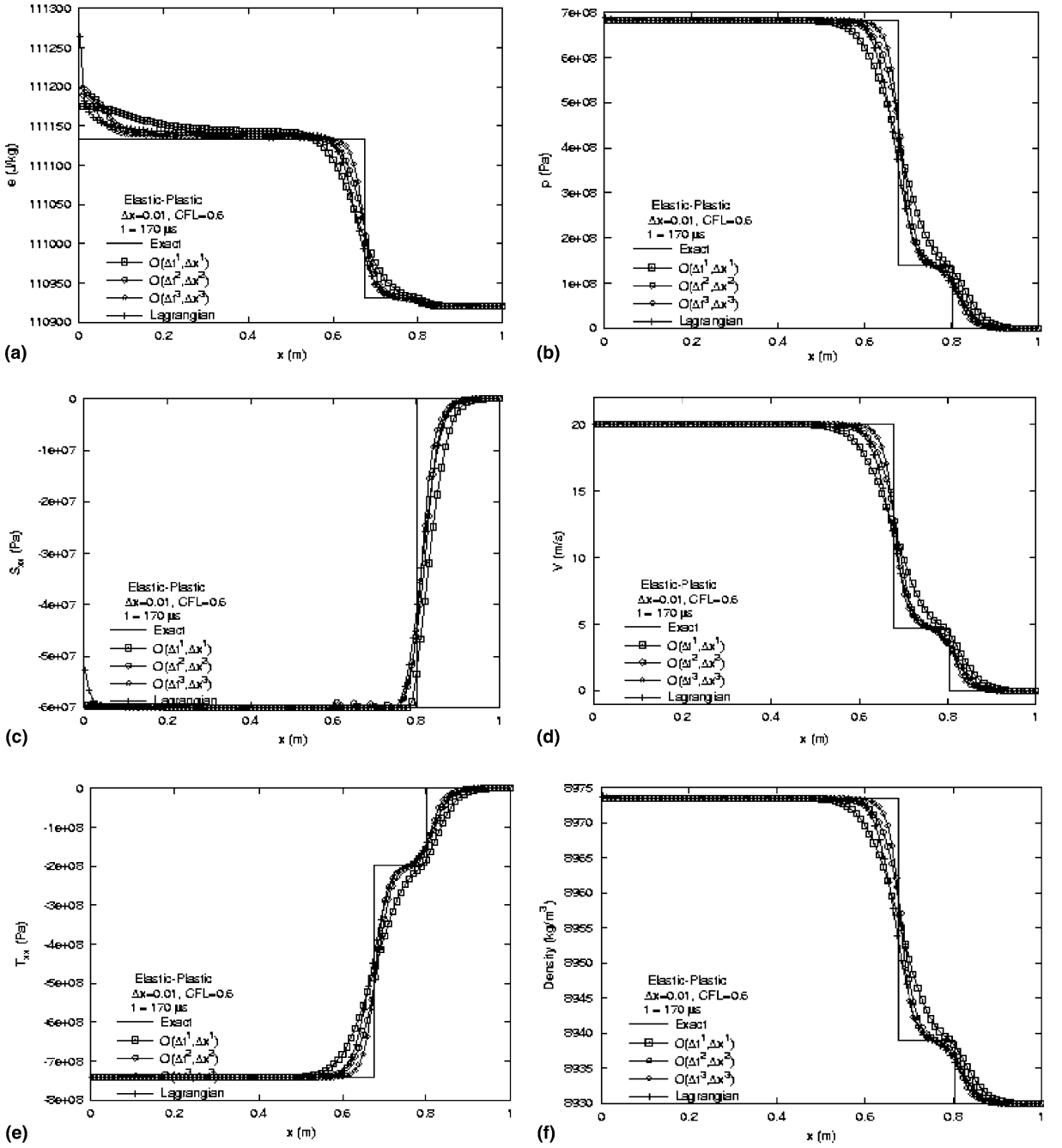

Fig. 10. Impact at 20 m/s on a copper rod. Impact takes place at the left end. The equations for elasto-plastic deformation are solved with the Mie–Gruneisen equation of state: (a) internal energy, (b) pressure (c) deviatoric stress, (d) velocity, (e) total stress, (f) density.

the hydrodynamic case. The deviatoric stress for the second-order solution shows some small oscillation near the shock. The Lagrangian deviatoric stress shows a slight error at the location of the initial discontinuity, which is related to a transient overshoot of pressure and velocity in the early stage of the solution. When the velocity overshoots, it results in a positive velocity gradient that allows the deviatoric stress to unload slightly from the yield surface. However, the Eulerian calculation does not seem to experience any such difficulty.

The effect of mesh resolution is shown for the second-order calculations in Figs. 11(a) and (b) and for the third-order calculations in Figs. 11(c) and (d). These figures give a close-up view of the elastic precursor and shock 200 μs after impact, and at a Courant number of 0.8. Results for the initial mesh spacing and 1/2, 1/4, 1/8, and 1/32 the original spacing are plotted. The results for both second- and third-order are evidently converging to the exact results, in terms of value and the shock locations. The internal energy, which shows errors near the impact boundary, does not show any error associated with the elastic–plastic wave. A comparison of the second-order with the corresponding third-order curve shows that in each case, the third-order result is more accurate as expected.

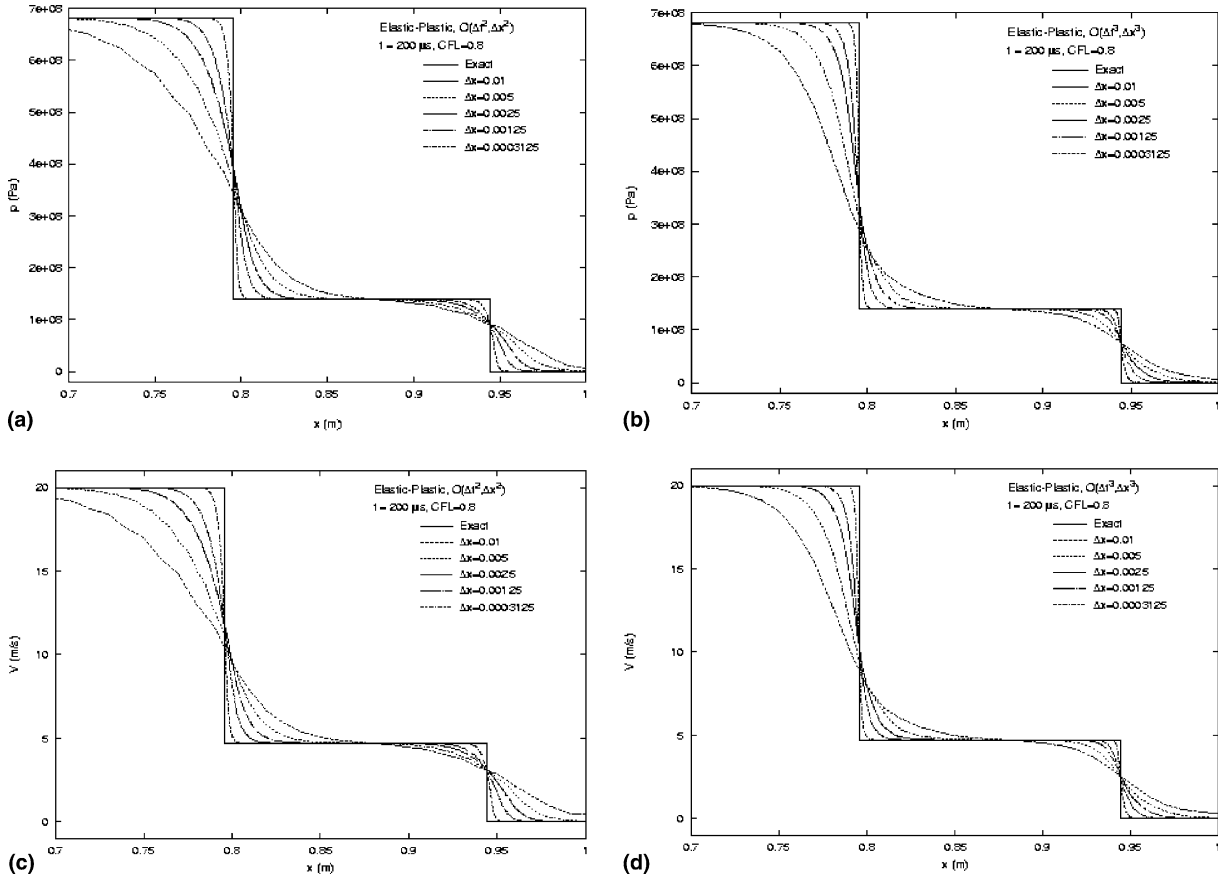

Fig. 11. Close-up view of pressure and velocity profiles near the shock for impact at 20 m/s on a copper rod. The convergence to the exact solution with mesh refinement is shown. Impact takes place at the left end. The equations for elasto-plastic deformation are solved with the Mie–Gruneisen equation of state: (a) pressure from a second-order scheme, (b) pressure from a third-order scheme, (c) velocity from a second-order scheme, (d) velocity from the third-order scheme.

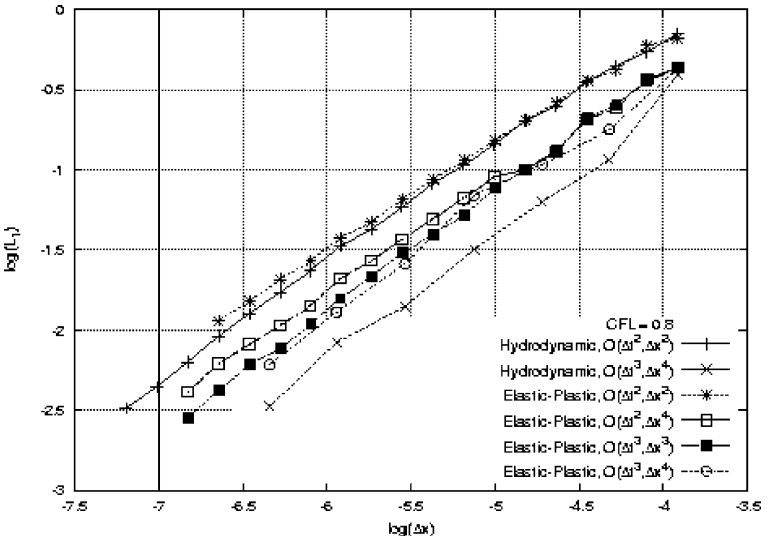

Fig. 12. Plot of log(error) against log(dx) for the one-dimensional calculations for shocks caused by impact in the different cases studied.

The convergence of the method for both hydrodynamic and elastic–plastic cases is shown in Fig. 12 Here, the L_1 norm of the error in velocity is plotted against mesh spacing. The norm is given by

$$L_1 = \int_{\text{body}} |v_{\text{calc}} - v_{\text{exact}}| \, \mathrm{d}x. \tag{72}$$

The slope of the curves indicates roughly first-order convergence, which is to be expected for this problem involving discontinuous exact solutions. The convergence rate is seen to be independent of the e.o.s. employed for the pressure and also independent of the material strength model. The figure gives results for a variety of orders of accuracy and introduces some mixed-order solutions, such as the $O(\Delta t^3, \Delta x^4)$ case which performed better than the third-order calculations for both hydrodynamic and elastic–plastic calculations. Similarly, switching to fourth-order spatial accuracy with second-order time accuracy improved the results at any given spatial resolution.

The one-dimensional calculations have verified that the numerical scheme correctly captures both hydrodynamic and elastic–plastic waves. In addition, higher-order accuracy, up to third-order in time and fourth-order in space, improves the accuracy of the solution for a given mesh size and time step size.

7.3. Investigation of effect of limiters on shock sharpening

In the above cases, it was observed that the problems with impact contained several points in the shock, even for the third-order accurate schemes. We conducted a systematic study of the effect of the e.o.s and the limiter (minmod in all the above cases) on the sharpness of the shocks obtained. From the above results it appears that the conventional LLF-ENO scheme with minmod limiter captures very crisp shocks for the Euler equations for ideal gases while its performance is less impressive for the same system with the Mie–Gruneisen equation of state. In the latter case the shocks appear to be diffused more. To investigate the possibility of using more compressive limiters to sharpen the shock we tried two other limiters. For any point in the domain, located at say x_j, we compute the fluxes at the cell face location, say $x_{j+1/2}$ using the standard LLF-ENO flux computation outlined in Section 5. The choice of the convex ENO flux is then

performed using a limiter. Different limiters would apply different extents of dissipation at the location of large gradients. The three limiters chosen for study are written in general form (see [6]) as follows. Define:

$$r_j^+ = \frac{(\Delta_- f(q_j) + \alpha_{j+\frac{1}{2}} \Delta_- q_j)}{(\Delta_+ f(q_j) + \alpha_{j+\frac{1}{2}} \Delta_+ q_j)}, \tag{73}$$

$$r_j^- = \frac{(\Delta_- f(q_{j+1}) + \alpha_{j+\frac{1}{2}} \Delta_- q_{j+1})}{(\Delta_+ f(q_{j+1}) + \alpha_{j+\frac{1}{2}} \Delta_+ q_{j+1})}, \tag{74}$$

where

$$\Delta_\pm q_j = \pm(q_{j\pm1} - q_j). \tag{75}$$

Now the limiters choose between the fluxes at the cell face $x_{j+1/2}$ by means of the switches:

$$\text{Minmod}: \ \phi_{\text{MM}}(r) = \max(0, \min(r, 1)), \tag{76}$$

$$\text{Superbee}: \ \phi_{\text{SB}}(r) = \max(0, \min(2r, 1), \min(r, 2)), \tag{77}$$

$$\text{VanLeer}: \ \phi_{\text{VL}}(r) = \frac{r + |r|}{1 + |r|}. \tag{78}$$

As described by Liu and Osher [6] the limiters are compressive in the following order: MM < VL < SB. When second-order fluxes are being compared there are two choices for flux in each direction at the cell face. Then the above procedure provides the algorithm for effecting a choice. When third-order fluxes are being computed there are three choices from each direction at the cell face and then the limiter has to be applied recursively to choose the appropriate flux.

We now compute cases of impact to study the effects, on the sharpness of the captured shocks for given order of accuracy due to:

1. impact velocity;
2. equation of state;
3. limiter (we use the abbreviations LLF-ENO-MM, LLF-ENO-SB, and LLF-ENO-VL for the minmod, superbee, and VanLeer limiters, respectively).

7.3.1. The Sod problem

First, the effects of the limiters on shock capturing for the Euler equations with gamma law gas dynamics are shown in Fig. 13 The pressure ratio of 10 and density ratio of 8 is set initially, with air as the material. The results at a specific instant are shown for the minmod ((a), (b)), superbee ((c), (d)), and VanLeer ((e), (f)) limiters. For this case, the shock is captured well (with three points in the shock) by all three limiters with second- and third-order accurate schemes. However, the overcompressive superbee limiter appears to lead to oscillations at the rarefaction wave, and the contact discontinuity. The VanLeer limiter is well behaved at the shock but shows slight undershoot at the rarefaction. Thus, for ideal gases the minmod limiter for the LLF-ENO performs well when compared to the other two limiters. In any case, for this problem, since the shock is captured in a sufficiently small number of points even with the LLF-ENO-MM scheme, there is no need for any remedy. We contrast this with a Sod problem run on a solid material, i.e., the Euler equations are again solved, but with the Mie–Gruneisen equation of state for the pressure. The material chosen for this test is HMX, a solid energetic material. The data for this case were obtained from Arienti et al. [57]. In their work an approximate Riemann solver was employed to solve the problem shown in Fig. 14 The shock was captured in about four mesh points. While the current ENO-based solver is much

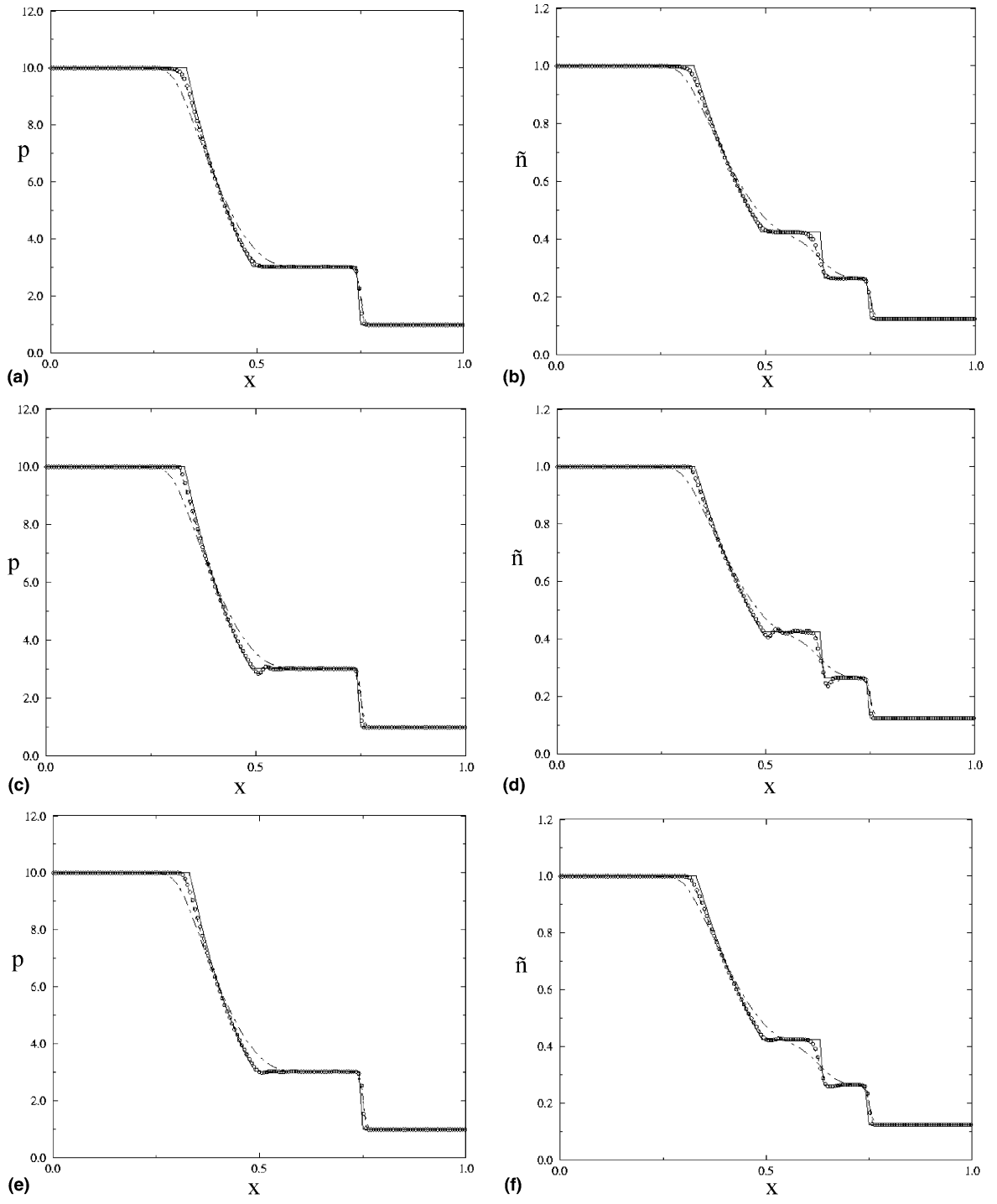

Fig. 13. Sod problem for ideal gas solved with the LLF-ENO with three different limiters: (a) pressure (LLF-ENO-MM), (b) density (LLF-ENO-MM), (c) pressure (LLF-ENO-SB), (d) density (LLF-ENO-SB), (e) pressure (LLF-ENO-VL), (f) density (LLF-ENO-VL). Solid line, exact; dot-dashed, first-order; dashed, second-order; circles, third-order.

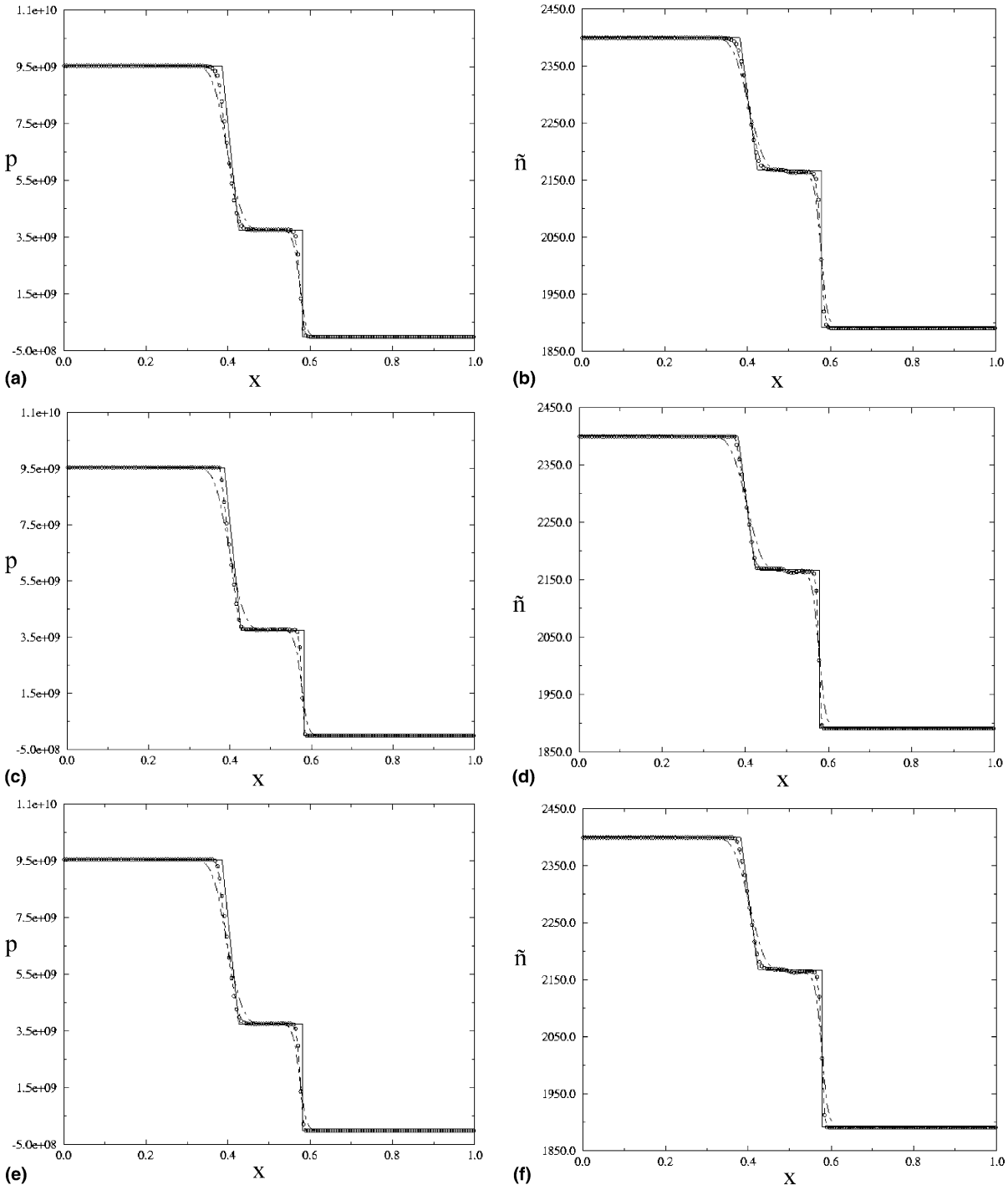

Fig. 14. Sod problem for a solid (Euler equations with Mie–Gruneisen equation of state) solved with the LLF-ENO with three different limiters: (a) pressure (LLF-ENO-MM), (b) density (LLF-ENO-MM), (c) pressure (LLF-ENO-SB), (d) density (LLF-ENO-SB), (e) pressure (LLF-ENO-VL), (f) density (LLF-ENO-VL). Solid line, exact; dashed, first-order; circles, second-order; triangles, third-order.

simpler to construct, even for the multidimensional case, since it does not employ field-by-field decomposition, the shock is somewhat more diffuse with a minmod limiter. This is shown in Figs. 14(a) and (b). In Fig. 14(a) we show that the second- and third-order ENO schemes with minmod limiter lead to about six points in the shock. Note that two of these points lie at the head and foot of the shock. This behavior is not observed in the previous case (Fig. 13), i.e., for the gamma law gas. Note that the weak contact discontinuity is picked up by the LLF-ENO-MM simulation. Using the more compressive LLF-ENO-SB solver gives a sharper shock with only three points in the shock (Figs. 14(c) and (d)). Note that the rarefaction and contact discontinuity are also picked up in sharper fashion. The results for the LLF-ENO-VL (Figs. 14(e) and (f)) are intermediate between LLF-ENO-MM and LLF-ENO-SB.

7.3.2. 1D impact problem

We next look at the impact problem and the effect of impact velocity and limiter type on the solutions of impact problems. The first example shown in Fig. 15 is of impact in the hydrodynamic situation, i.e., the Euler equations are solved with the Mie–Gruneisen e.o.s. The impact velocity here is low, i.e., 20 m/s. It is noticed that the LLF-ENO-MM solution (Figs. 15(a) and (b)) shows a very diffuse shock (18 points for the second-order and 14 points for the third-order). In Figs. 15(c) and (d) we show the results from LLF-ENO-SB. The shock is much crisper here and there are about 6 points in the shock for the second- and third-order schemes. Note that in each of the above cases a number of points lie at the head and foot of the shock. The LLF-ENO-VL scheme is again intermediate between the MM and SB limited schemes. The diffusion at the shock is clearly dependent on the impact velocity as shown in Fig. 16. This is a case of 2000 m/s impact, again for the Euler equations with Mie–Gruneisen e.o.s. Here, there are far fewer points in the shock when compared to the low velocity impact case. LLF-ENO-MM gives shocks with seven and five points, respectively, for second- and third-order schemes (Figs. 16(a) and (b)). While the LLF-ENO-SB scheme (Figs. 16(c) and (d)) gives a very crisp shock with only about three points for second- and third-order schemes, small oscillations in the flow behind the shock are observed in this case. The LLF-ENO-VL (Figs. 16(e) and (f)) scheme gives solutions with about four points within the shock and the solutions are oscillation-free.

In Fig. 17 we show results from calculations of impact with an elasto-plastic material. The full equations for uniaxial strain are solved with elastic-perfectly plastic material. The Mie–Gruneisen e.o.s is used for pressure. This case has the classic two-wave structure with a fast-moving weaker elastic precursor followed by the plastic wave. The performance of the various schemes is essentially the same as that for the gamma law gas, indicating that the material model does not influence the dissipation at the shock. In Figs. 17(a) and (b) we show the results from LLF-ENO-MM calculation. The plastic and elastic wave locations and strengths are correctly captured by the method. There are about 18(14) points in the plastic and 12(11) points in the weak elastic precursor for second- (third-) order scheme. The plastic and elastic waves are close enough that the two waves are completely diffused by the first-order scheme. When the LLF-ENO-SB scheme was used for this case, the shock was captured sharply with 10(8) and 6(5) points in the plastic and elastic shocks with second- (third-) order scheme. However, the strength of the elastic precursor was incorrectly predicted by this more compressive scheme. The LLF-ENO-VL scheme was somewhat more accurate than the LLF-ENO-MM and also correctly captured the elastic precursor.

In summary, the LLF-ENO scheme of Liu and Osher [6], i.e., with minmod limiter was found to be somewhat diffusive when the Euler equations are solved using the Mie–Gruneisen e.o.s. for pressure. The material model did not appear to influence this tendency to spread the shocks. The diffuseness of the shock is more severe for the low impact velocities, where the disparity between particle and shock speed is higher. This indicates that the diffusion at the shock, which leads to several points in the head and foot region of the shock, is due to the disparity between the particle and shock speeds in the case of solid materials. To remedy this, we attempted to use limiters of higher compressibility than LLF-ENO-MM. The more

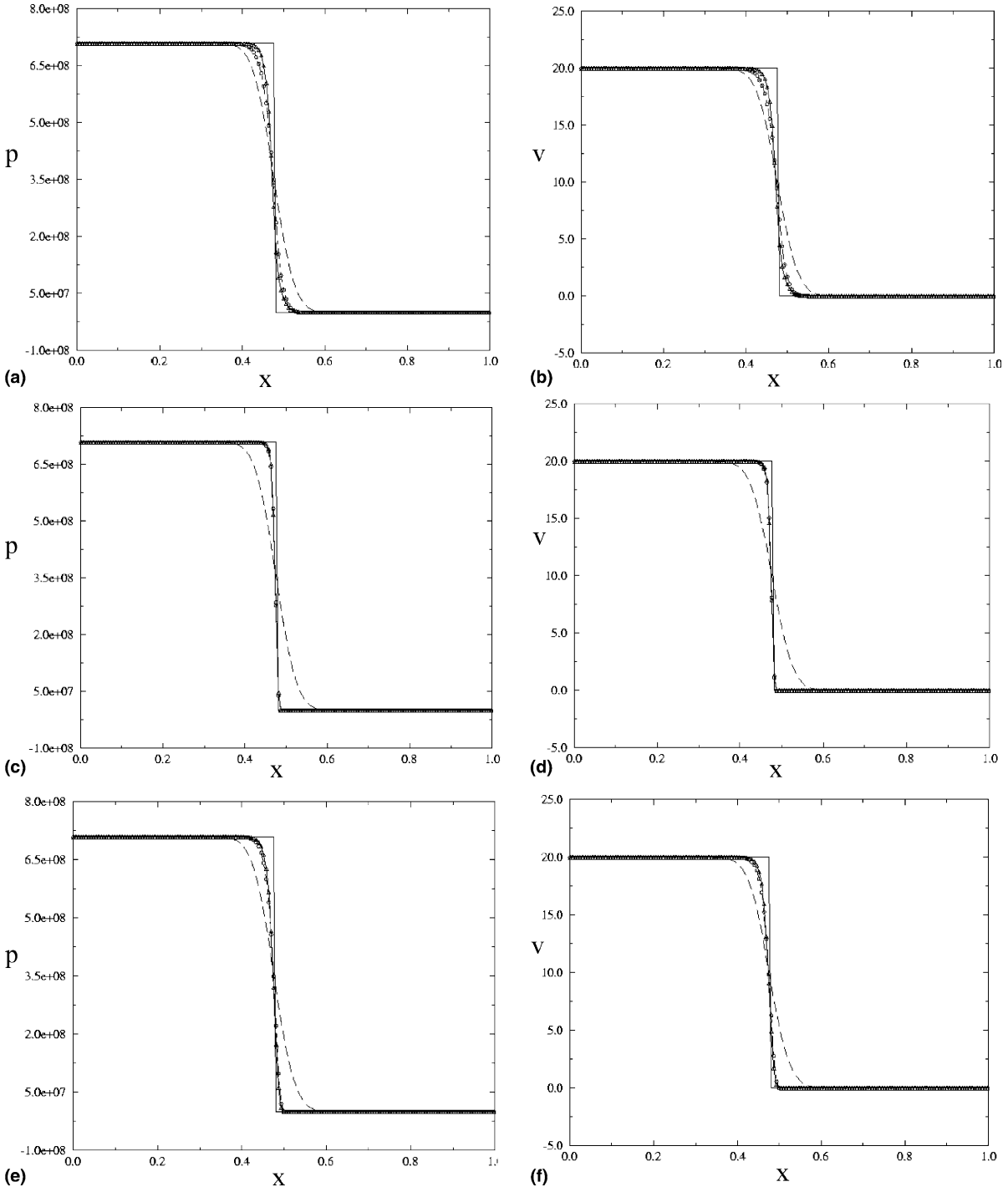

Fig. 15. Impact problem (20 m/s impact velocity) for ideal gas solved with the LLF-ENO with three different limiters: (a) pressure (LLF-ENO-MM), (b) velocity (LLF-ENO-MM), (c) pressure (LLF-ENO-SB), (d) velocity (LLF-ENO-SB), (e) pressure (LLF-ENO-VL), (f) velocity (LLF-ENO-VL). Solid line, exact; dashed, first-order; circles, second-order; triangles, third-order.

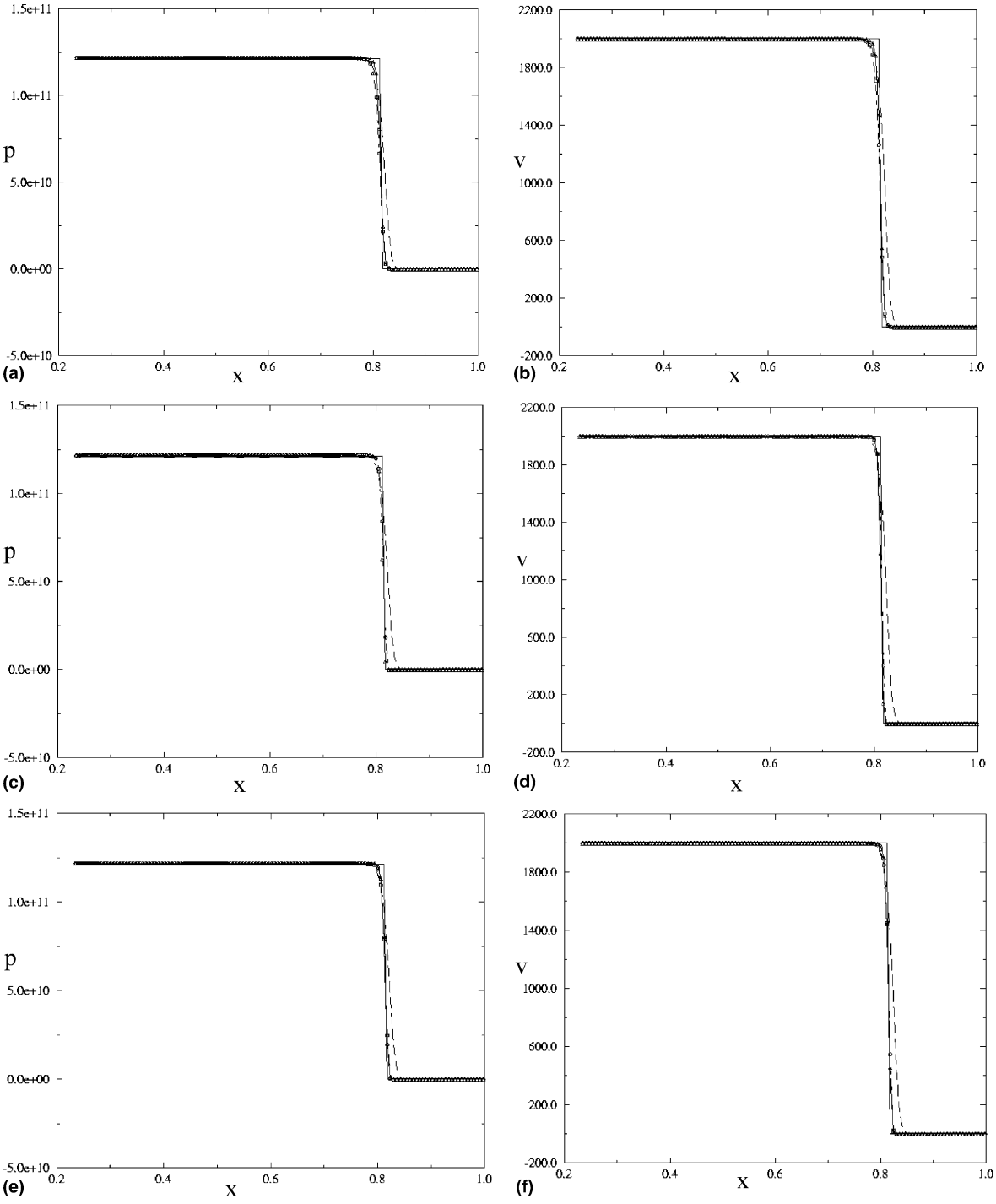

Fig. 16. Impact problem (2000m/s impact velocity) for ideal gas solved with the LLF-ENO with three different limiters: (a) pressure (LLF-ENO-MM), (b) velocity (LLF-ENO-MM), (c) pressure (LLF-ENO-SB), (d) velocity (LLF-ENO-SB), (e) pressure (LLF-ENO-VL), (f) velocity (LLF-ENO-VL). Solid line, exact; dashed, first-order; circles, second-order; triangles, third-order.

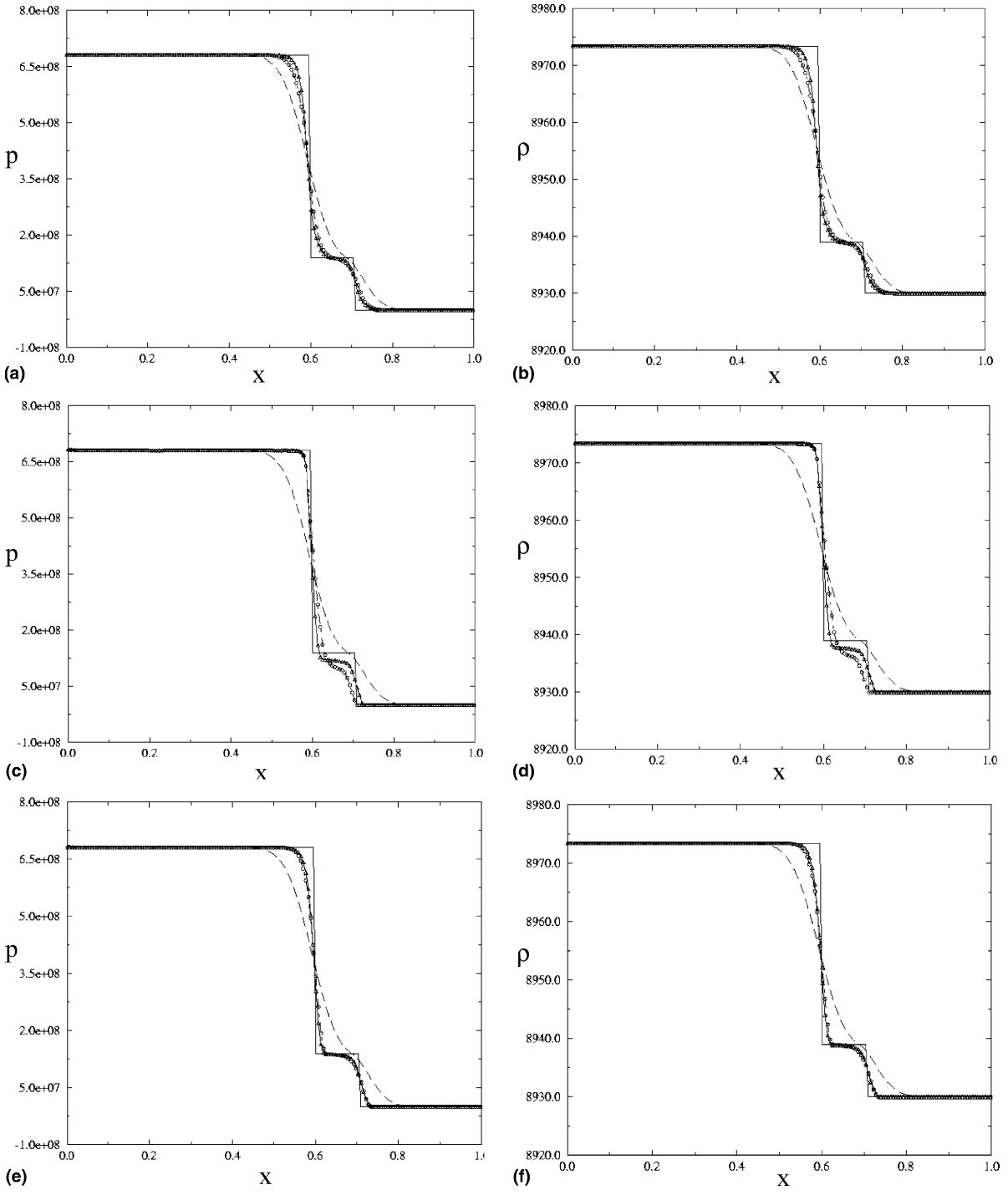

Fig. 17. Impact problem for an elasto-plastic solid solved with the LLF-ENO with three different limiters: (a) pressure (LLF-ENO-MM), (b) density (LLF-ENO-MM), (c) pressure (LLF-ENO-SB), (d) density (LLF-ENO-SB), (e) pressure (LLF-ENO-VL), (f) density (LLF-ENO-VL). Solid line, exact; dashed, first-order; circles, second-order; triangles, third-order.

compressive superbee limiter gave unphysical results for the elasto-plastic material case and weakly oscillatory results in other cases. The LLF-ENO-VL scheme gave some improvement over the LLF-ENO-MM. However, in the gasdynamic situation, the VL limiter also gave undesirable undershoots. We also computed the 2D cases shown in a later section with the LLF-ENO-VL scheme and found little difference from the LLF-ENO-MM calculations for schemes of equal nominal order of accuracy. Thus, for the present, despite its less than satisfactory shock resolution characteristics, the LLF-ENO-MM scheme is used in all the results presented.

8. Two-dimensional calculations

8.1. The axisymmetric Taylor impact problem

We now compare our calculations of the axisymmetric Taylor impact problem with a benchmark. Here, we will only present the axisymmetric cases. The computations are performed on a uniform Cartesian mesh covering the domain. The vertical (y-) axis is the symmetry axis. Initially the impactor, a copper rod, and the flat rigid surface were placed some distance apart on the mesh. The material properties chosen were: young's modulus $E = 117$ GPa, density of copper $= 8930$ kg/m^3, poisson's ratio $v = 0.35$, yield stress $=$ 400 Mpa. Impact was initiated by prescribing a rigid body velocity to the copper rod. Initially there is a region of void between the two interfaces. This void disappears at impact to form the material–material interface between the copper rod and the rigid impacted surface. When the interface markers lie in a material–void region of the interface we apply the boundary conditions of type 2 (MV) on such markers. On markers in the material–material portions of the interface, b.c.'s of type 1 (MM) are applied. Note that the discretization procedure in the multidimensional case requires the value of q_{int} at the interface location, which may not be coincident with the interfacial markers. The values at such points on the interface are obtained by using local quadratic interpolants to fit the interface values stored at the marker points for each

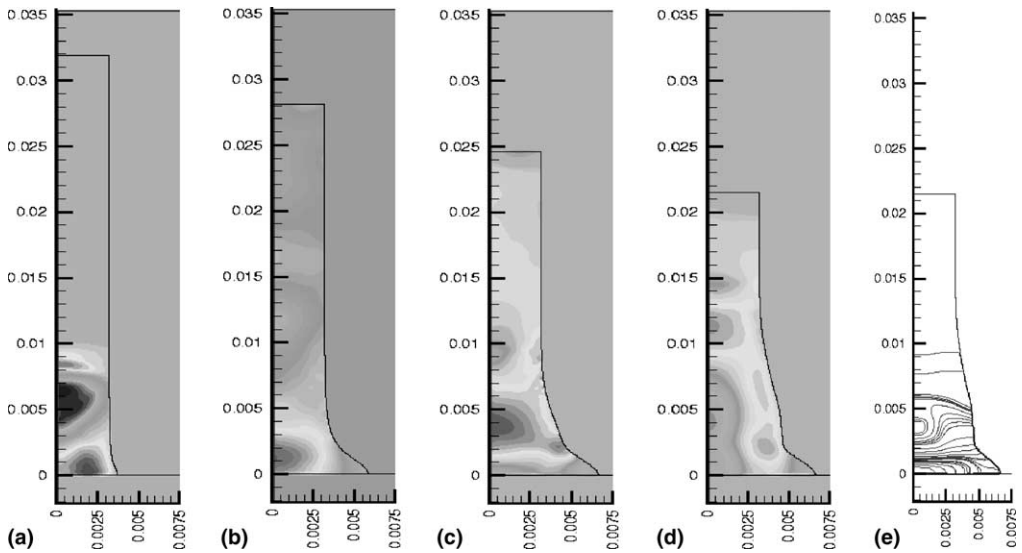

Fig. 18. Axisymmetric deformation of a copper rod impacting a rigid surface with avelocity of 227 m/s. The pressure contours and interface shapes are shown at four instants of time after impact: (a) $t = 2.5$ μs, (b) $t = 20$ μs, (c) $t = 40$ μs, and (d) $t = 80$ μs. Also shown in (e) are the contours of plastic strain when the bar finally comes to rest, i.e., at $t = 80$ μs after impact.

variable. These interface values at markers are computed depending on whether the points are MM or MV points, from Eqs. (52a) to (59f).

Figs. 18(a)–(d) show the interface shapes and pressure contours for impact of the copper rod translating downward at 227 m/s (as benchmarked in [12]). Figs. 18(a)–(d) show the bar at $t = 2.5$, 20, 40, and 80 μs after impact. The bar is nearly at rest at the last instant shown, i.e., at 80 μs. This value for time of rest agrees very well with the time of rest predicted by Camacho and Ortiz. Thus, the calculation correctly predicts the rate of conversion of kinetic energy to plastic work. The maximum width of the mushroom formed after impact is 6.8 mm. The values obtained by the various authors fall in the range of 6.97–7.24 [12]. The present method slightly underpredicts the final mushroom extent. This discrepancy could perhaps be due to the fixed grid nature of our calculations, where the mesh resolution at the instant of impact may not be sufficient to fully resolve the large gradients at the material–material interface. In the Lagrangian approach of Camacho and Ortiz, an adaptive mesh refinement technique is used. In particular, the edge of the mushroom at the base appears to be slightly more blunt in our case than the corresponding result shown in [12]. The height of the rod after impact is obtained from our calculations to be 21.4 mm. This value agrees exactly with the Camacho and Ortiz's value. The other features in agreement with the benchmark are the two bulges in the final deformed shape. The extent of these bulges and the time after impact at which they appear is in excellent agreement with Camacho and Ortiz. In Fig. 18(e), we show the plastic strain contours in the final shape. The distribution of strains is in good overall agreement with Camacho and Ortiz. In particular, the present method predicts a trough in the plastic strain contour plot centered between 3 and 4 mm from the rigid surface at the symmetry axis. This location of the trough is also shown by the results of Camacho and Ortiz [12].

In Figs. 19(a)–(d), we show the interface shapes and pressure contours for impact of copper rod at a higher velocity of 400 m/s. The interface and pressure contours are shown at four instants after impact, i.e., $t = 2.5$, 20, 40, and 100 μs. The rod comes to rest at about 100 μs after impact. The features of the final shape, including the extended mushroom at the base and the location and extent of the bulge above the mushroom are in good qualitative agreement with experimentally obtained shapes of impacted copper rods as pictured in [2]. In Fig. 20, we compare the relative extents of deformation of the final shapes of the rod after impact at the two velocities computed, i.e., at 227 and 400 m/s. In each case, the mushrooming of the base occurs early during the impact (the first 20 μs). Following that, as the plastically deformed base hardens, the second bulge begins to form.

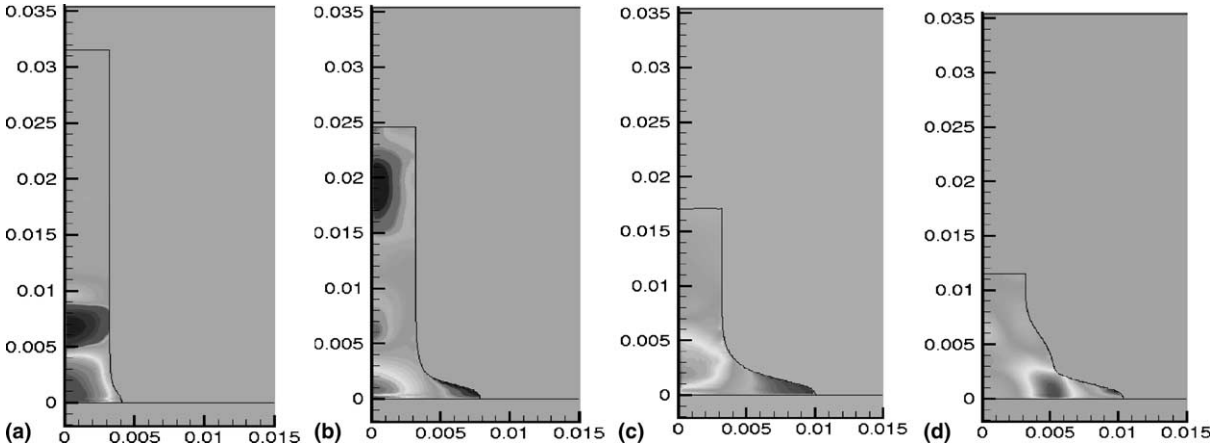

Fig. 19. Axisymmetric deformation of a copper rod impacting a rigid surface with a velocity of 400 m/s. The pressure contours and interface shapes are shown at four instants of time after impact: (a) $t = 2.5$ μs, (b) $t = 20$ μs, (c) $t = 40$ μs, and (d) $t = 100$ μs.

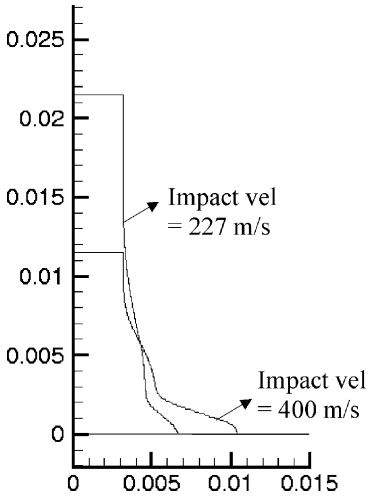

Fig. 20. Comparison of computed final shapes of the copper rod for impact at 227 and 400 m/s.

8.2. Impact between two deformable surfaces

As a final demonstration, we examine the case of high-velocity impact of one deformable object onto a deformable surface. This case is shown in Fig. 21, where we calculate the impact of a cylinder with a plane surface. Both surfaces are copper and the material properties in the model correspond to elasto-plastic deformation of the metal. In the figure, we show on the left the contours of velocity magnitude in the impactor and the target along with the velocity vectors in the flow domain. On the right we show contours of equivalent stress. Also shown in each of the figures is the shape of the boundaries of the two materials. As can be seen in these figures there is an abrupt transition in the corners from a material–material interface to a material–void interface for each material. Appropriate boundary conditions as discussed in Section 7 are applied in these regions. Zero-gradient conditions are applied at the sides of the domain assuming that the target has infinite extent in all except the $+y$ direction. Figs. 21 (a)–(c) correspond to time instants 2.5, 50, and 100 μs after impact, respectively. The progression of the elasto-plastic waves and the formation of large gradients in the velocity as well stress fields is evident from the figure. At the rim of the impactor, the interfaces are constantly in collision since the material–void interfaces are being pushed against each other to form material–material interfaces. Thefore the rim of the impact region registers large stress and correspondingly, large strain values. Stress waves are propagated into the materials from this point. In Fig. 21(c) it can be seen that the velocity field is such as to continuously push the impactor into the target leading to the production of an upswell in the target material around the rim. This is also indicated clearly by the velocity vectors shown. Regions of compression and tension are seen from the contours of stress. Fig. 21(c) shows the final resting shape of both the target and impactor. The magnitudes of the velocity in the final frame are very small. The computational time for a 100×100 mesh calculation to the stage shown in Fig. 21(c) is about one hour on a Hewlett Packard B-2000 workstation. No attempt has been made to optimize the code and it should be possible to decrease computational times significantly.

9. Summary and future work

We have described the development of a numerical technique based on a fixed-grid sharp interface tracking approach for the simulation of multi-material impact. The physics of the problem is such that

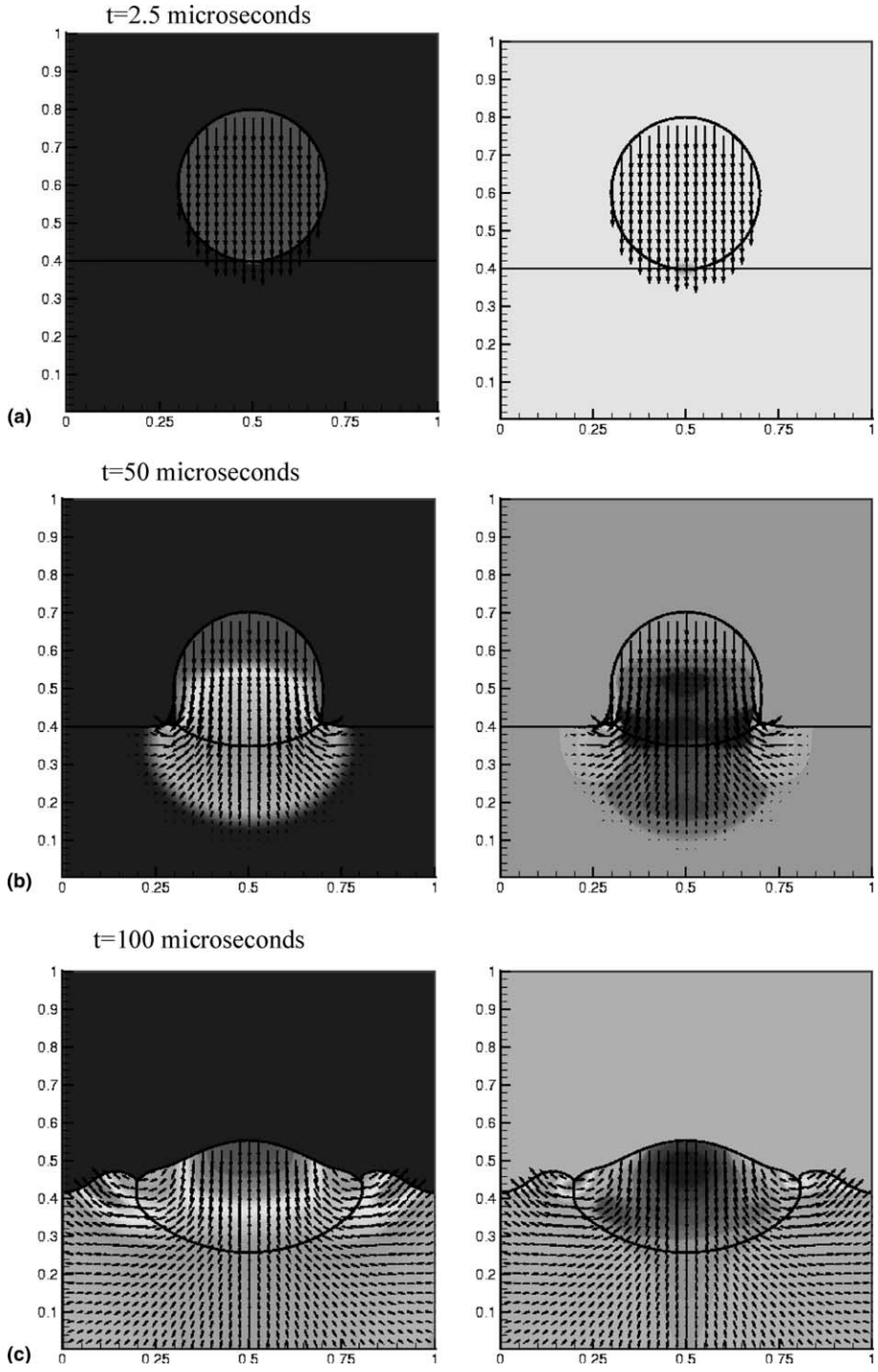

Fig. 21. Impact of a cylinder with a planar surface. The cylinder impacts the target with a velocity of 2000 m/s directed downward. The figures on left show velocity contours and vectors along with the interface shapes. The times after impact are indicated alongside the figures. The figures on right show stress contours.

nonlinear elasto-plastic wave-propagation phenomena occur in the materials leading to the formation of shocks. We track interfaces explicitly as curves in 2D. In its interaction with the flowfield, although we are computing on a fixed mesh, the interface is treated sharply and the discontinuities at the interface are not smeared. We have demonstrated that the current method has the following capabilities:

(1) The interface can be tracked through large distortions.
(2) Accurate shock-capturing schemes can be implemented for Cartesian grids and extended in a straightforward manner to incorporate the presence of the moving interfaces.
(3) Boundary conditions are applied at the exact locations of the boundaries.
(4) Different regions of the boundaries can have different boundary conditions, i.e., the material–material and material–void boundary conditions. These are applied at the interface points identified to lie in regions where the interfaces are in contact and where the interface is exposed to void, respectively. These boundary conditions are physically dictated or numerical boundary conditions. The suitability of the set of b.c.'s is determined based on numerical experimentation. The singularity resulting from an abrupt transition from a material–material to material–void b.c. at the interfaces is handled well.
(5) Computations of the deformation process are carried to large distortions while the interfaces travel through the mesh in a stable and robust manner.

Benchmark calculations performed for the Taylor impact problem demonstrated that the method successfully captured the dynamics of the impact, including the time of deformation and the final shapes of the object at the end of impact.

In ongoing work several extensions of the methodology presented in this paper are in progress. To enable simulation of dynamic response of energetic materials, we have included rate-dependent effects by replacing the elasto-plastic model with the Johnson–Cook model containing rate-dependent effects. Using the level-set technique we have computed the collapse of voids in materials subject to shocks due to impact, while maintaining a sharp interface treatment. Under this framework extension to three-dimensions is relatively straightforward and is in progress

References

[1] J.A. Zukas, T. Nicholas, H.F. Swift, L.B. Gresczuk, D.R. Curran, Impact Dynamics, Wiley, New York, 1982.
[2] M.A. Meyers, Dynamic Behavior of Materials, Wiley, New York, 1994.
[3] A. Harten, B. Engquist, S. Osher, S.R. Chakravarthy, uniformly high-order accurate essentially non-oscillatory schemes, III, J. Comp. Phys. 131 (1997) 3–47.
[4] C.-W. Shu, S. Osher, Efficient implementation of essentially non-oscillatory shock-capturing schemes, J. Comp. Phys. 77 (1988) 439–471.
[5] C.-W. Shu, S. Osher, Efficient implementation of essentially non-oscillatory shock-capturing schemes II, J. Comp. Phys. 83 (1989) 32–78.
[6] X.-D. Liu, S. Osher, Convex ENO high order schemes without field-by-field decomposition or staggered grids, J. Comp. Phys. 142 (1998) 304–330.
[7] T. Ye, R. Mittal, H.S. Udaykumar, W. Shyy, An accurate Cartesian grid method for viscous incompressible flows with complex immersed boundaries, J. Comp. Phys. 156 (1999) 209–240.
[8] H.S. Udaykumar, R. Mittal, P. Rampunggoon, A. Khanna, An Eulerian–Lagrangian Cartesian grid method for simulating flows with complex moving boundaries, J. Comp. Phys. 174 (2001) 1–36.
[9] D.J. Benson, Computational methods in Lagrangian and Eulerian hydrocodes, Comput. Meth. Appl. Mech. Eng. 99 (1992) 235–395.
[10] W.-K. Liu, T. Belytschko, H. Chang, An arbitrary Lagrangian–Eulerian finite element method for path-dependent materials, Comput. Meth. Appl. Mech. Eng. 58 (1986) 227–245.
[11] G.T. Camacho, M. Ortiz, Computational modeling of impact damage in brittle materials, Int. J. Solids Struct. 33 (1996) 2899–2938.
[12] G.T. Camacho, M. Ortiz, Adaptive Lagrangian modeling of ballistic penetration of metallic targets, Comput. Meth. Appl. Mech. Eng. 142 (1997) 269–301.
[13] A. Duarte, J.T. Oden, An *h–p* adaptive method using clouds, Comput. Meth. Appl. Mech. Eng. 139 (1996) 237–262.

[14] G.R. Johnson, R.A. Stryk, S.R. Beissel, SPH for high velocity impact computations, Comput. Meth. Appl. Mech. Eng. 139 (1996) 347–373.
[15] W.-K. Liu, S. Hao, T. Belytschko, S. Li, C.T. Chang, Multi-scale methods, Int. J. Numer. Meth. Eng. 47 (7) (2000).
[16] T. Belytschko, Y. Guo, W.-K. Liu, S.P. Xiao, Unified stability analysis of meshless particle methods, Int. J. Numer. Meth. Eng. 48 (9) (2000).
[17] J. Dolbow, John, N. Moes, T. Belytschko, Discontinuous enrichment in finite elements with a partition of unity method, Finite Elements Anal. Des. 36 (3) (2000).
[18] N. Moes, J. Dolbow, T. Belytschko, Finite element method for crack growth without remeshing, Int. J. Numer. Meth. Eng. 46 (1) (1999) 131–150.
[19] N. Sukumar, N. Moes, B. Moran, T. Belytschko, Extended finite element method for three-dimensional crack modelling, Int. J. Numer. Meth. Eng. 48 (2000) 1549–1570.
[20] C.W. Hirt, B.D. Nichols, Volume of fluid (VOF) method for the dynamics of free boundaries, J. Comp. Phys. 39 (1981) 201.
[21] C.S. Peskin, Numerical analysis of blood flow in the heart, J. Comp. Phys. 25 (1977) 220–252.
[22] J. Glimm, J. Grove, B. Lindquist, O.A. McBryan, G. Tryggvason, The bifurcation of tracked scalar waves, SIAM J. Sci. Stat. Comput. 1 (1988) 61–79.
[23] H. Braes, P. Wriggers, Arbitrary Lagrangian Eulerian finite element analysis of free surface flow, Comput. Meth. Appl. Mech. Eng. (2000) 95–109.
[24] L.B. Lucy, A numerical approach to the testing of the fission hypothesis, Astron. J. 82 (12) (1977) 1013–1024.
[25] J.J. Monaghan, An introduction to SPH, Comput. Phys. Commun. 48 (1988) 89–96.
[26] G.A. Dilts, Moving-least-squares-particle hydrodynamics I. Consistency and stability, Int. J. Numer. Meth. Eng. 44 (1999) 1115–1155.
[27] P.W. Randles, L.D. Libersky, Normalized SPH with stress points, Int. J. Numer. Meth. Eng. 48 (2000) 1445–1462.
[28] R. Vignjevic, J. Campbell, L. Libersky, A treatment of zero-energy modes in the smoothed particle hydrodynamics method, Comput. Meth. Appl. Mech. Eng. 184 (2000) 67–85.
[29] J.K. Chen, J.E. Beraum, C.J. Jih, An improvement for tensile instability in smoothed particle hydrodnamics, Comput. Mech. 23 (1999) 279–287.
[30] N.R. Aluru, A reproducing kernel particle method for meshless analysis of microelectromechanical systems, Comput. Mech. 23 (1999) 324–338.
[31] J.K. Chen, J.E. Beraun, T.C. Carney, A corrective smoothed particle method for boundary value problems in heat conduction, Int. J. Numer. Meth. Eng. 46 (1999) 231–252.
[32] G.A. Dilts, Moving least-squares particle hydrodynamics II: conservation and boundaries, Int. J. Numer. Meth. Eng. 48 (2000) 1503–1524.
[33] J.P. Morris, P.J. Fox, Y. Zhu, Modeling low Reynolds number incompressible flows using SPH, J. Comp. Phys. 136 (1997) 214–226.
[34] R. Scardovelli, S. Zaleski, Direct numerical simulation of free surface and interfacial flow, Ann. Rev. Fluid Mech. 31 (1999) 567.
[35] C. Beckermann, H.J. Diepers, I. Steinbach, A. Karma, X. Tong, Modeling melt convection in phase-field simulations of solidification, J. Comp. Phys. 154 (1999) 468–496.
[36] J.A. Trangenstein, A second-order algorithm for the dynamic response of soils, Impact Computing Sci. Eng. 2 (1990) 1–39.
[37] J.A. Trangenstein, A second-order algorithm for two-dimensional solid mechanics, Comput. Mech. 13 (1994) 343–359.
[38] J.A. Trangenstein, Adaptive mesh refinement for wave propagation in nonlinear solids, SIAM J. Sci. Comput. 16 (1995) 819–939.
[39] J.A. Trangenstein, R.B. Pember, The Riemann problem for longitudinal motion in an elastic–plastic bar, SIAM J. Sci. Stat. Comput. 12 (1991) 180–207.
[40] G.H. Miller, P. Colella, A high-order Eulerian Godunov method for elastic–plastic flow in solids, J. Comp. Phys. 167 (1) (2001) 131–176.
[41] D.J. Benson, A multi-material Eulerian formulation for the efficient solution of impact and penetration problems, Comput. Mech. 15 (1995) 558–571.
[42] S.R. Cooper, D.J. Benson, V.F. Nesterenko, A numerical exploration of the role of void geometry on void collapse and hot spot formation in ductile materials, Int. J. Plasticity 16 (2000) 525–540.
[43] D.M. Anderson, G.B. McFadden, A.A. Wheeler, Diffuse interface methods in fluid mechanics, Ann. Rev. Fluid Mech. 30 (1998) 139–165.
[44] D.J. Benson, A mixture theory for contact in multi-material Eulerian formulations, Comput. Meth. Appl. Mech. Eng. 140 (1997) 59–86.
[45] R. Menikoff, E. Kober, Compaction waves in granular HMX, Los Alamos National Lab Report, LA-13456-MS, 1999.
[46] R. Menikoff, Errors when shock waves interact due to numerical shock width, SIAM J. Sci. Stat. Comput. 15 (5) (1994) 1227–1242.
[47] S. Chen, B. Merriman, S. Osher, P. Smereka, A simple level set method for solving Stefan problems, J. Comput. Phys. 135 (1) (1997) 8–29.

[48] T.Y. Hou, Z. Li, S. Osher, H. Zhao, A hybrid method for moving interface problems with application to the Hele–Shaw flow, J. Comp. Phys. 134 (2) (1997) 236–247.
[49] X.-D. Liu, R.P. Fedkiw, M. Kang, A boundary condition capturing method for Poisson's equation on irregular domains, J. Comput. Phys. 160 (1) (2000) 151–178.
[50] H.S. Udaykumar, W. Shyy, M.M. Rao, Elafint: a mixed Eulerian–Lagrangian method for fluid flows with complex and moving boundaries, Int. J. Numer. Meth. Fluids 22 (1996) 691.
[51] H.S. Udaykumar, R. Mittal, W. Shyy, Solid–liquid phase front computations in the sharp interface limit on fixed grids, J. Comput. Phys. 153 (1999) 535–574.
[52] R.P. Fedkiw, T. Aslam, B. Merriman, S. Osher, A non-oscillatory eulerian approach to interfaces in multimaterial flows (the ghost fluid method), J. Comput. Phys. 152 (1999) 457–492.
[53] R.P. Fedkiw, Coupling an Eulerian fluid calculation to a Lagrangian solid calculation with the ghost fluid method, J. Comput. Phys. 175 (2002) 200–224.
[54] M. Kang, R. Fedkiw, X.-D. Liu, A boundary condition capturing method for multiphase incompressible flow, J. Sci. Comput. 15 (2000) 323–360.
[55] R.J. Leveque, Z. Li, The immersed interface method for elliptic equations with discontinuous coefficients and singular sources, SIAM J. Numer. Anal. 31 (4) (1994) 1019–1044.
[56] S. Osher, J.A. Sethian, Fronts propagating with curvature dependent speed: algorithms based in Hamilton–Jacobi formulations, J. Comp. Phys. 79 (1988) 12–49.
[57] M. Arienti, E. Morano, J. Shepherd, Nonreactive Euler flows with Mie–Gruneisen equation of state for high explosives, 1999. Available from www.caltech.edu/~eric/Papers/FM99-8.pdf.
[58] R.P. Fedkiw, A. Marquina, B. Merriman, An isobaric fix for the overheating problem in multimaterial compressible flows, J. Comp. Phys. 148 (1999) 545–578.
[59] P. Glaister, An approximate Riemann solver for the Euler equations for real gases, J. Comp. Phys. 74 (1988) 382–408.
[60] J.K. Dukowicz, A general, non-iterative Riemann solver for Godunov's method, J. Comp. Phys. 61 (1985) 119–137.
[61] G.H. Miller, E.G. Puckett, A high-order Godunov method for multiple condensed phases, J. Comp. Phys. 128 (1996) 134–164.
[62] K.J. Vanden, Characteristic analysis of the uniaxial stress and strain governing equations with thermal-elastic and Mie–Gruneison equation of state, Technical Memorandum, AFRL, Eglin AFB, Eglin, FL, 1998.
[63] J.A. Trangenstein, P. Collela, A high-order Godunov method for modeling finite deformation in elastic–plastic solids, Comm. Pure Appl. Math. 44 (1991) 41–100.
[64] G.-S. Jiang, C.-W. Shu, Efficient implementation of weighted ENO schemes, J. Comp. Phys. 126 (1996) 202–228.
[65] R. Donat, A. Marquina, Capturing shock reflections: an improved flux formula, J. Comp. Phys. 125 (1996) 42–58.